



Hydrodynamic Porosity: A Paradigm Shift in Flow and Contaminant Transport Through Porous Media, Part I

August H. Young^{1,2}, Zbigniew J. Kabala³

5 ¹ Duke Center for WaSH-AID, Durham, NC, 27701, USA

² Mechanical Engineering and Materials Science, Duke University, Durham, NC, 27710, USA

³ Civil and Environmental Engineering, Duke University, Durham, NC, 27710, USA

Correspondence to: August H. Young (ahf12@duke.edu)

Abstract

10 Pore-scale flow velocity is an essential parameter in determining transport through porous media, but it is often miscalculated. Researchers use a static porosity value to relate volumetric or superficial velocities to pore-scale flow velocities. We know this modeling assumption to be an *oversimplification*. The variable fraction of porosity conducive to flow, what we define as *hydrodynamic porosity*, θ_{mobile} , exhibits a quantifiable dependence on Reynolds number (i.e., pore-scale flow velocity) in the Laminar flow regime. This fact remains largely unacknowledged in the literature. In this work, we quantify the dependence of

15 θ_{mobile} on Reynolds number via numerical flow simulation at the pore scale. We demonstrate that, for the chosen cavity geometries, θ_{mobile} decreases by as much as 42% over the Laminar flow regime. Moreover, θ_{mobile} exhibits an *exponential* dependence on Reynolds number. The fit quality is effectively perfect, with a coefficient of determination (R^2) of approximately 1 for each set of simulation data. Finally, we show that this exponential dependence can be easily solved for pore-scale flow velocity through use of only a few Picard iterations, even with an initial guess that is 10 orders of magnitude

20 off. Not only is this relationship a more accurate definition of pore-scale flow velocity, but it is also a necessary modeling improvement that can be easily implemented.

Keywords: *Hydrodynamic Porosity, Cavity, Dead-End Pore, Pore Velocity, Volumetric Velocity, Reynolds Number, Groundwater Remediation*

1 Introduction

25 Groundwater is a primary drinking water source for 38% and 50% of the domestic and global populations, respectively (The Nature Conservancy, 2022). Despite mankind's undeniable dependence on clean groundwater, we have failed to properly protect it from anthropogenic pollutants. In the United States, the EPA Superfund Program oversees 1,336 sites on the agency's National Priorities List; another 40 sites are proposed to be added to this list (United States Environmental Protection Agency, 2023). Of the additional sites regulated by the Office of Environmental Management, there exists a total of 6.5 trillion liters of



30 contaminated groundwater (equaling roughly 4 times the country’s daily water consumption) and 40 million cubic meters of
contaminated soil (Office of Environmental Management, 2023a). The organization will spend 529 million USD remediating
that volume of contaminated soil and groundwater in 2024 (Office of Environmental Management, 2023b).

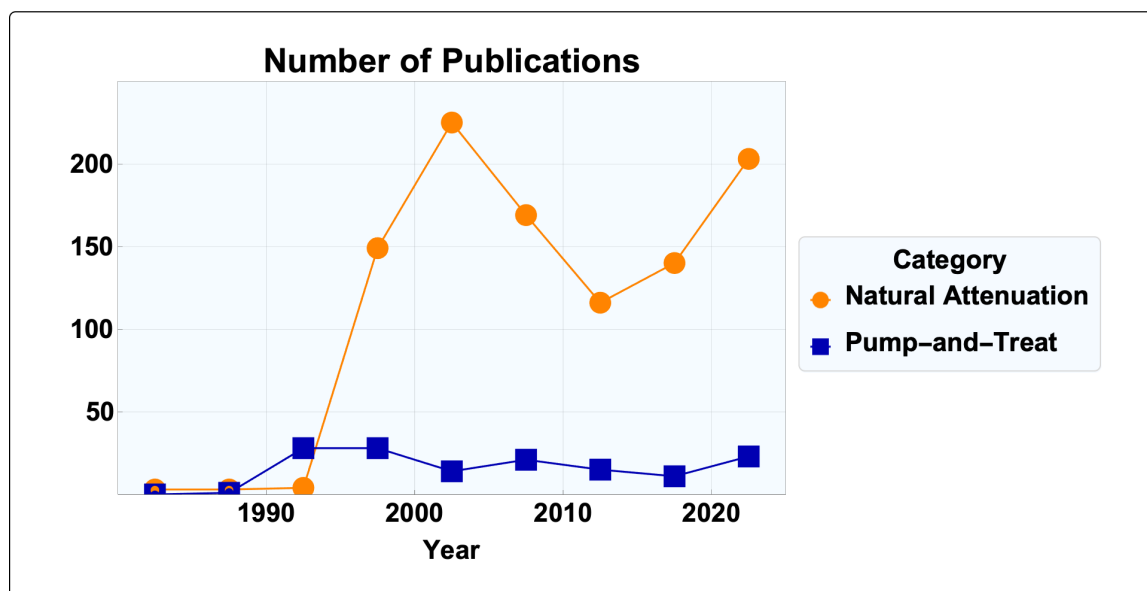
Groundwater pollution is not just a pressing issue in the United States. For example, the Chinese State Council recently
35 announced a groundwater remediation initiative equivalent to 5.5 billion USD. Though costly, the price for inaction is even
higher: with 70% of the population dependent on groundwater, and 90% of shallow sources polluted (37% of which to the
extent that they cannot be restored to drinking water quality, according to the Chinese Ministry of Land and Resources), 190
million Chinese residents fall ill every year, and 60,000 die, directly, or indirectly from groundwater contamination (Qiu,
2011).

40 The national groundwater cleanup debt for the United States was last estimated three decades ago at as much as 1 trillion USD
by Russell et al. (1991) and highlighted by the National Resource Council (NRC). Adjusting for inflation, that’s approximately
2 trillion USD in groundwater remediation debt today. We believe that a comprehensive, updated estimate would be larger –
perhaps by an order of magnitude. At the time of the previous estimate, the NRC also emphasized that the rate of discovery
45 of contaminated sites “far exceeded” the rate of cleanup (McCarty, 1990). Even more notably, these cost estimates were made
before discoveries of the contaminants that have emerged over the last 25 – 30 years and those that have resurfaced due to
seemingly boundless prior use. Examples of such contaminants include fluorinated chemicals, known as PFAS, agricultural
products, and cleaners. But these are just a few – researchers estimate that a total of eight million synthetic and naturally
occurring chemicals were used in industrial, commercial, agricultural, and military activities over the past two centuries
50 (National Research Council, 2000). Further counteracting remediation efforts are phenomena that slow remediation efforts and
result in contaminant rebound, e.g., DNAPL and matrix diffusion (Hadley and Newell, 2012). Still, other contributors arise
from sources of geological contaminants (e.g., lead, arsenic, and other heavy metals), inadequate modeling of contaminant
plumes, funding caps, and, of course, our inability to stop polluting. Altogether, these phenomena elongate remediation
timeframes, and as a result, increase the associated cost.

55 With the bleak picture of our groundwater cleanup debt seemingly growing bleaker every year, it is unsurprising that
practitioners, as well as government and funding agencies, increasingly embrace monitored natural attenuation (i.e., natural
processes such as biodegradation, sorption, dilution, dispersion, and other chemical reactions that decrease contaminant
concentrations) as an alternative to active treatment methods like pump-and-treat remediation. When conditions are favorable,
60 monitored natural attenuation should be considered as an alternative to energetically and economically expensive active
remediation schemes. But these conditions are rare, and monitored natural attenuation is only appropriate for contaminants
and sites that can be properly characterized over time.



Despite the shortcomings of natural attenuation, there has been a paradigm shift in the approach to groundwater remediation – from active strategies (i.e., pump-and-treat) toward passive approaches (i.e., monitored natural attenuation). The study and implementation of monitored natural attenuation grew rapidly in popularity since the 1990s; the same cannot be said for pump-and-treat research, which remained relatively stagnant (see Figure 1). Evidence of this paradigm shift is materialized in publications that provide guidance for the natural attenuation of PFAS, popularly known as “forever chemicals” (Newell et al., 2021), and contaminants that are recognizably difficult to treat via natural attenuation (e.g., gasoline additives such as methyl tert-butyl ether) (National Research Council, 2000). By 2000, The National Academies Press noted that natural attenuation was approved “more and more frequently” despite a limited scientific understanding of the processes involved, the potential risks, and the fact that it does not utilize continuously operated and supervised cleanup systems (National Research Council, 2000).



75

Figure 1: Number of publications produced by title searches for “natural attenuation” (blue) and “pump-and-treat” (yellow) indexed by Web of Science in 5-year bins (1980-1984, 1985-1989, ..., 2015-2019, 2020-2024); title search results are for February 28, 2023, with the contents of the last bin extrapolated from 2020 to this date.

Because the definition of natural attenuation includes the dispersion and dilution of contaminants (National Research Council, 2000), it becomes an attractive, low-effort, low-cost alternative to active remediation strategies. The National Academies Press highlights this reality, citing Arulanantham (1998): “Investigators and regulators sometimes employ and advocate minimalist criteria or rules of thumb to make quick decisions on natural attenuation without using detailed technical protocols to show cause and effect.” Pressure comes from site owners, who know that the cost savings of natural attenuation can be in the millions (USD) (National Research Council, 2000). Powers (1996) found that natural attenuation was 12 million USD less expensive than a conventional pump-and-treat system at the French Limited site in Houston. But this is just for one site, suggesting far

85



more substantial savings for national corporations and agencies responsible for multiple site locations. Regrettably, monitored natural attenuation is usually a spurious alternative to pump-and-treat remediation, offering polluters the opportunity to skirt their cleanup responsibilities. Resulting, is the passage of our current groundwater remediation debt onto future generations.

90 In this work, we intend to reverse the observed paradigm shift in groundwater remediation strategy and resurrect the utilization of pump-and-treat systems. We justify this call by highlighting the fact that contaminated groundwater resources can be remediated at a *fraction* of formerly estimated costs. This is because remediation timeframes for pump-and-treat systems were previously estimated for *steady flows* and a *static definition of porosity* – a definition based on the mainstream, but outdated, single-porosity, double-porosity, and Mobile-Immobile Zone porosity models. The modeling of hydrodynamic porosity,
95 θ_{mobile} , as a flow-dependent parameter is a *paradigm shift* in the understanding of flow and transport in porous media. The outdated Mobile-Immobile Zone model (wherein θ_{mobile} is assumed to be constant) is still in popular use today (e.g., consider the recent publications in leading journals: *Water Resources Research* (Li et al., 2022), *Environmental Science & Technology* (Zhou et al., 2023), *Journal of Hydrology* (Kwaw et al., 2023), *Groundwater* (Toyama et al.), etc.). The result is a poor presentation of induced subsurface flows and an overestimation of remediation costs.

100

Kahler and Kabala recently highlighted these potential cost-savings by demonstrating that remediation timeframes can be reduced by close to an *order of magnitude* for unwashed media (e.g., fractured rock and glacial deposits) subject to a rapidly pulsed flow; first via numerical simulation (Kahler and Kabala, 2016), then by physical experimentation (Kahler and Kabala, 2019). These results apply to contaminant removal from, as well as bacteria and nutrient delivery to, the dead-ended pore
105 spaces in unwashed media. And they offer hope that the national groundwater cleanup debt could be cut by almost an order of magnitude (a factor of seven, to be exact). For example, if we estimate that 30% of our contaminated groundwater formations are primarily unwashed media and assume that these formations would otherwise be cleaned by steady pump-and-treat, we would be looking at a cost savings of approximately 100 billion USD if we were to instead use rapidly pulsed pump-and-treat.

110 To utilize the cleanup process discovered by Kahler and Kabala (2016) (i.e., the deep sweeps and vortex ejections that manifest themselves only in rapidly pulsed pumping), we introduce a new concept, *hydrodynamic porosity*, θ_{mobile} , to refer to the variable fraction of porosity used to transmit fluid through porous media. Without doing so, we cannot properly model the base flow that underlies the pulsations. For example, the predominant operational mode of pump-and-treat utilizes a circulation well that results in a dipole flow field, e.g., see Dinkel et al. (2020); Xia et al. (2019); Thomson et al. (2008); Sutton et al.
115 (2000); Kabala (1993); Kabala and Xiang (1992). In this flow pattern, velocities (and therefore Reynolds numbers) vary by orders of magnitude along flow streamlines. We illustrate this variation in Figure 2 below, by using the velocity field quantified by Philip and Walter (1992) for a confined, isotropic aquifer of infinite extent. For the highlighted streamline, we observe a four-order-of-magnitude change in the normalized pore-scale flow velocity. As qualitatively noted by Li et al. (1996) and Kabala and Kim (2011), changes in flow velocity result in changes to the volume of void space that is conducive to flow.



120 *Missing from the scientific literature is the explicit relationship between hydrodynamic porosity, θ_{mobile} , and pore-scale flow*
velocity (or interstitial Reynolds number).

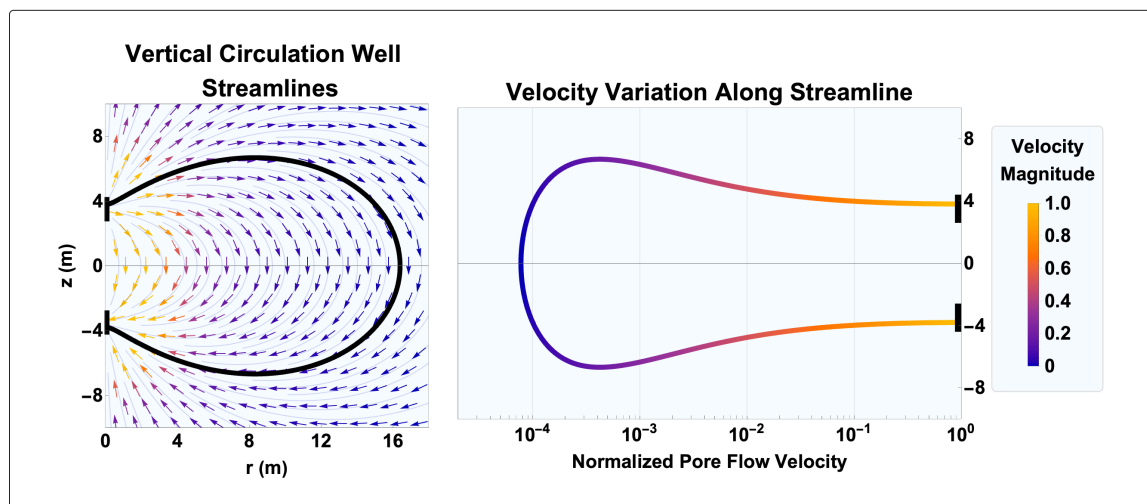


Figure 2: Vertical circulation well streamlines for a confined, isotropic aquifer, mathematically described by Philip and Walter (1992) (left). Normalized velocity variation along the vertical coordinate of the streamline highlighted in black (right).

125 Addressing this gap in the literature requires that we quantify and establish a relationship between hydrodynamic porosity,
 θ_{mobile} , and flow velocity (Reynolds number). Given this relationship, researchers could determine the magnitude of the
modeling errors that result when θ_{mobile} is replaced by a static parameter. The magnitude of these errors is especially
consequential to decision-making calculations (i.e., those that pertain to the timescales and costs of remediation projects). In
our subsequent work, we demonstrate the magnitude of the error that results when θ_{mobile} is replaced by a static parameter for
130 induced subsurface flows (such as the vertical circulation well we illustrate above).

2 Related Work

2.1 Effective Porosity

In this work, we introduce a new concept, *hydrodynamic porosity*, θ_{mobile} , to refer to the variable portion of porosity able to
transmit fluid through porous media. As we later demonstrate, θ_{mobile} varies with pore-scale flow velocity near sharp edges
135 and dead-end pores. We choose to use this term because it is not imbued with other, previously defined meanings. It differs
from that of dynamic porosity, which describes the shrinking or swelling of porous media (Sheng et al., 2019; McDonald et
al., 2020) dynamic effective porosity, which describes variably saturated porous media around the capillary fringe (Luo et al.,
2023); and effective porosity, which is used by authors to describe a multitude of context-dependent phenomena.

Warranting further discussion is the concept and definition of effective porosity – a term commonly encountered in the study
140 of porous media flows. Researchers define effective porosity as the portion of constant porosity used to transmit fluid through



porous media. Although we could have used this work to describe the *hydrodynamic nature of effective porosity*, we refrain from using the term *effective porosity* due to its many alternative definitions that cloud the term in unnecessary ambiguity. Take, for example, the definition of effective porosity assigned by the textile industry. In the context of hernia meshes, effective porosity is meant to define changes to the pore morphology after implantation of the mesh in situ (Jacombs et al.,
145 2020). This is quite different from the definition used by Sevee (2010) in a study on the effective porosity of marine clay. In this study, effective porosity describes the void space in the clay that participates in advective transport. Still, other definitions describe it as the difference between the total porosity minus the soil water content at 0.33 bar (Helalia, 1993; Timlin et al., 1999). Readers are directed to Hapgood et al. (2002), Flint and Selker (2003), Cartwright et al. (2009), and Ma et al. (2022) for additional, alternative definitions. Given the highly varied use of effective porosity, we instead adopt the more precise
150 term, hydrodynamic porosity, θ_{mobile} .

Among the authors that define effective porosity as the portion of constant porosity used to transmit fluid through porous media are Li et al. (1996), Kabala and Kim (2011), Kim (2006), Lindsay (1994), and Werth (2013). Here, we note that while these authors qualitatively consider its hydrodynamic nature, they do not quantify it. For example, Li et al. (1996) qualitatively
155 note the dependence of effective porosity on flow velocity in a study of sedimentary rock flows. The authors attribute the observed decrease to the presence of selective pathways (i.e., fissures and cracks) in the studied rock formation. They do not discuss an explicit relationship between what they term effective porosity and flow velocity. Further, the morphology of the rock formation studied in this work is starkly different than that of granular media.

In his doctoral dissertation at Duke, and a later publication with his advisor, Dr. Zbigniew Kabala, Kim (2006) and Kabala and Kim (2011) provide the most thorough discussion on the hydrodynamic quality of effective porosity; the authors state a dependence of effective porosity on both pore geometry and Reynolds number. They demonstrate this dependence in the same idealized pore space we study in this work using the FIDAP software. The authors show that effective porosity varies by at least an order of magnitude for creeping flows and postulate that it may “vary by as much” for non-creeping flows but do not
165 develop an explicit relationship between effective porosity and Reynolds number (Kabala and Kim, 2011).

Other authors have qualitatively considered the impact of dead-end pores on effective porosity. Lindsay (1994) notes that in water-saturated paper, flow can be restricted by mechanical obstructions in the form of isolated and dead-end pores. The author also discusses the development of stagnant zones in high Reynolds number flows, and the absence of these zones in creeping
170 flows due to the ability of the flow to closely follow abrupt changes in medium geometry. In effect, the author contemplates the dependence of effective porosity on Reynolds number but does not account for it in his analysis. The concept of flow-dependent porosity also appears in a study on baleen, though in a much different context. Werth (2013) describes a linear relationship between fringe porosity and incident flow velocity until a certain limiting velocity is reached, at which point the effective porosity of the baleen decreases. Given that the application of this work is to learn more about the mechanical



175 properties of baleen to better understand the feeding behaviors of various whale species, the spatial scale and flow path
morphology are fundamentally different than those studied in this work.

2.2 Cavity Flows

As we discuss in the next section, flow past cavities (also known as dead-end or blind pores), which serve as the theoretical
basis for this research, are a popular research topic and comparatively well-explored. There are ample publications concerning
180 contaminant transport and flow manipulation and instabilities in dead-end pores. The bulk of this work pertains to the geometric
manipulation of pore geometry to determine the effect on the induced flow (Moffatt, 1963; Higdon, 1985; Shen and Floryan,
1985; Fang et al., 1997). Other studies on flow modulation have also been published, though this work is relatively less
explored (Jana and Ottino, 1992; Howes and Shardlow, 1997; Horner et al., 2002; Kahler and Kabala, 2016). Most of this
work is geared at industry for the guise of expediting rate-limited manufacturing processes (e.g., etching, finishing, cleaning,
185 etc.) that are applied to surfaces with cavities (Chilukuri and Middleman, 1984; Alkire et al., 1990; Fang et al., 1999).

In this work, we leverage the same physical theory that describes flows past cavities to define a hydrodynamic porosity function
 $\theta_{mobile}(\mathbf{v}_{pore}) = \theta_{mobile}(Re)$. Previously, Kahler and Kabala (2016, 2018, 2019), used the same approach to describe
contaminant transport in porous media – likening duct or surface flow to flow through a series of well-connected pores, and
190 flow past grooves and cavities on surfaces to flow past dead-end pores in granular media. Such results are crucial to
understanding how phenomena like contaminant rebound in groundwater reservoirs post-remediation can be mitigated.
Although Kahler and Kabala implied the hydrodynamic nature of porosity, they did not quantify it. In this paper, we
demonstrate and quantify, explicitly, this relationship for the first time. We also illustrate the ease with which this relationship
can be incorporated into flow and contaminant transport models. To understand why contaminant rebound after traditional
195 pump-and-treat groundwater remediation takes place, and how it could be mitigated, researchers need to account for
hydrodynamic porosity, θ_{mobile} .

3 Physics

The idea of a medium having a singular porosity value is overly simplistic due to the many heterogeneities and time-dependent
processes that occur in porous media. In larger structures, such as groundwater reservoirs, macrostructures and preferential
200 flow paths yield large and sporadic variations in porosity. In the case of packed beds, which are typically bounded,
impermeable boundaries cause significant variations in porosity due to channeling effects at the wall. In rock formations, the
concept of dual porosity is used to describe the very different characteristics of the medium itself and the fractures that separate
the medium. Such morphologies require a definition of porosity with spatial dependence. Other pore-space reduction
mechanisms like compaction and solute aggregation and deposition change the morphology of a medium over time. These
205 processes require a definition of porosity that is accommodating of these types of time-dependent processes. Both definitions,



however, are only dependent on the physical characteristics of the medium, whether over time or for an unchanging medium. What these definitions fail to account for, is the *nature* of the flow through porous media.

3.1 Pore-Scale Flow Velocity

Hydrodynamic porosity, θ_{mobile} , is used to quantify transport through porous media. For example, because θ_{mobile} defines pore-scale flow velocity, and therefore the actual velocity field in porous media flows, Truex et al. (2017) utilize this parameter (although they utilize a static, effective porosity value) to calculate contaminant transport time. This is an improvement over the use of the volumetric velocity (also known as the superficial or Darcy/Forchheimer velocity), which is a hypothetical velocity equivalent to what would result from flow through an entire cross-section of the medium and not just its pore spaces:

$$\mathbf{v}_{volumetric} = \mathbf{v} = \frac{Q}{A} = \mathbf{q} \quad (1)$$

Where Q is the volumetric flow rate, A , is the cross-sectional area of the medium, and \mathbf{q} , is the “flux.” Neglecting inertial effects, Darcy's law relates the volumetric velocity to the pressure gradient applied to the medium (Brutsaert, 2005; Muljadi et al., 2016; Bear, 1975):

$$-\nabla p = \frac{\mu}{k} \mathbf{v} \Leftrightarrow -\nabla h = \frac{\mu}{k \gamma} \mathbf{v} \Leftrightarrow -\nabla h = \frac{1}{K} \mathbf{v} \quad (2)$$

Where p is the pressure, h is the pressure head, k is the permeability of the medium, K is the hydraulic conductivity, γ is the specific weight of the fluid, and μ is its viscosity. The equivalences we show here are to illustrate the preferred forms in oil and gas reservoir modeling (left) and groundwater hydrology (right). When inertial effects cannot be neglected, as is the case for high Reynolds number flows, we must utilize the quadratic correction term, introduced by Èstudes (1863) and Forchheimer (1901). Given this adjustment, Darcy's law becomes the Forchheimer-Dupuit law:

$$-\nabla p = \frac{\mu}{k} \mathbf{v} + B \rho \mathbf{v}^2 \mathbf{n} \Leftrightarrow -\nabla h = \frac{1}{K} \mathbf{v} + B \frac{1}{g} \mathbf{v}^2 \mathbf{n} \quad (3)$$

where \mathbf{n} is a unit vector in the direction of the volumetric velocity, ρ the flow density, and B , a coefficient that can be found experimentally (Chen et al., 2015). Depending on the flow conditions, the volumetric velocity can be estimated experimentally from Eq. (2) or Eq. (3) (i.e., from Darcy's law or the Forchheimer-Dupuit law, respectively). To attain the true pore-scale flow velocity, which would be needed to determine quantities such as contaminant transport time, the volumetric velocity must be modified by the medium's porosity (Bear, 1975):

$$\mathbf{v}_{pore} = \frac{\mathbf{v}}{\theta} \quad (4)$$



In this formulation, θ is the effective porosity of the medium. Back-of-the-envelope calculations may simply use the total porosity of the medium. This would also be suitable for washed media without any cavities or other effectively immobile zones. Equation (4) can be derived from a simple conservation of mass analysis:

$$v_{pore} A_{pore} = v A \Leftrightarrow v_{pore} = \frac{A}{A_{pore}} v \Leftrightarrow v_{pore} = \frac{1}{\theta} v$$

235 Given our previous discussion, we know that use of the medium's total porosity is an oversimplification. Pore-scale flow velocity should instead be defined by the total volume that is conducive to flow (i.e., what we later refer to as mobile zones) – a quantity that is itself dependent on pore-scale flow velocity. Eq. (4) should instead read:

$$v_{pore} = \frac{v}{\theta_{mobile}(v_{pore})} = \frac{v}{\theta_{mobile}(Re)} \quad (5)$$

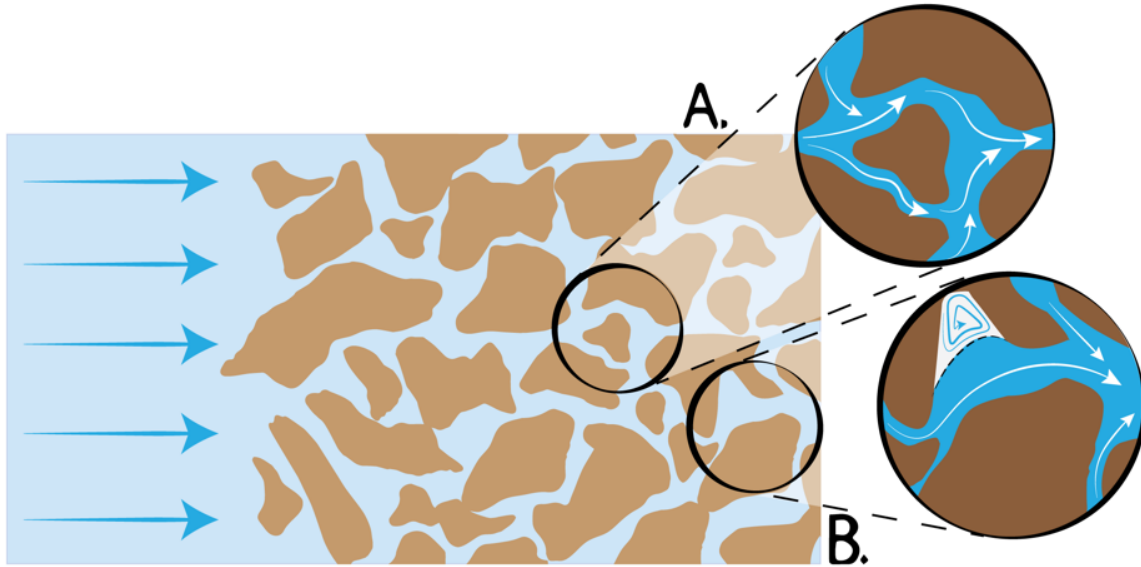
240 Where θ_{mobile} is itself a function of pore-scale flow velocity. The implicit nature of Eq. (5), while seemingly more difficult to solve than Eq. (4), is quickly resolved by a few Picard iterations. Not only is Eq. (5) a more accurate description of pore-scale flow velocity, but it is also a necessary improvement in the modeling of induced subsurface flows that can be easily implemented.

3.2 Mobile-Immobile Zone Model

245 Porous media can be broken down into two regions: mobile and “immobile” zones, as described by Vangenuchten and Wierenga (1976) in application to groundwater flows. In the mobile zone, solute transport occurs via advection and dispersion. The immobile zone is defined by isolated volumes of cavities or dead-ended pore space adjacently located to well-connected, mobile regions. In these zones, fluid recirculates in eddies, and solute transport is limited to the mechanism of vortex-enhanced diffusion. By this definition, the “immobile” label is a misnomer – fluid in the cavity space is *technically* mobile; it does not, however, move *through* the pore space. Thus, the fluid in this zone remains immobile *relative* to the flow in the mobile zone.

250

We illustrate these zones for an arbitrary matrix subject to an imposed flow in Figure 3, below. Magnification “A” provides an example of a mobile zone, and magnification “B” contains an example of an immobile zone in the form of a dead-end pore. The model we use to study this dead-end pore volume is discussed further in Section 3.5.



255 **Figure 3: Mobile zone composed of well-connected pore space (A), and an immobile zone in the form of a poorly connected/dead-end pore (B).**

3.3 Definitions of Porosity

The total porosity of a medium, θ , is defined by the cumulative volume of the mobile and immobile zones; and more specifically, as the ratio of the total pore space volume to the total volume of the media. In an isotropic or 2D medium, like the
 260 ones we study in this work, this definition can be written in terms of cross-sectional areas:

$$\theta = \frac{V_{pore}}{V} = \frac{A_{pore}}{A} \quad (6)$$

We note that $V = V_{bulk} = V_{total}$ and $A = A_{total}$. In the analysis that follows, we represent the pore volume (or area) by the dead-end pore model, which we illustrate in Figure 4. As a result, the pore volume can be defined in terms of mobile and
 265 immobile zones. Again, we provide the cross-sectional area expression for an isotropic medium or 2D media.

$$V_{pore} = V_{mobile} + V_{immobile} \rightarrow A_{pore} = A_{mobile} + A_{immobile} \quad (7)$$

Thus, we can define the *hydrodynamic porosity* of the medium, θ_{mobile} , by dividing Eq. (7) by the total volume of the medium, V (or cross-sectional area, A):

$$\theta = \frac{V_{mobile} + V_{immobile}}{V} = \theta_{mobile} + \theta_{immobile} \quad (8)$$



270 3.4 Defining the Pore-Space Partitioning Coefficient

Given that the pore space can be broken down into mobile and immobile zones, we can define a *pore-space partitioning coefficient*, ξ , to describe the ratio of pore space conducive to through-flow:

$$\xi = \frac{V_{mobile}}{V_{pore}} = \frac{A_{mobile}}{A_{pore}} \quad (9)$$

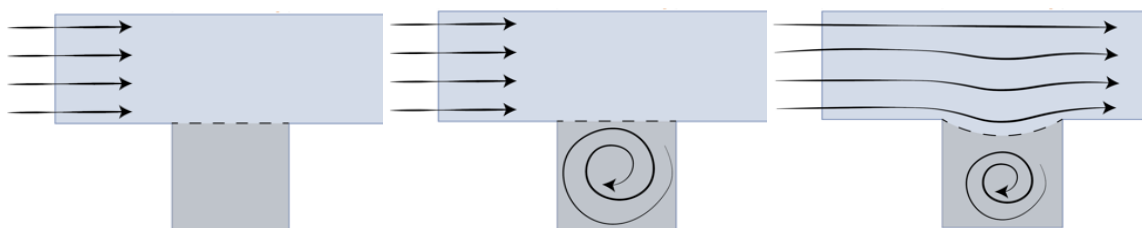
We note that the pore-space partitioning coefficient is related to the hydrodynamic porosity of the medium, θ_{mobile} , by:

$$275 \quad \xi = \frac{V_{mobile}}{V_{pore}} = \theta_{mobile} \frac{V}{V_{pore}} = \frac{\theta_{mobile}}{\theta} \quad (10)$$

In the analysis that follows, it is the *behavior of the pore-space partitioning coefficient* that we numerically quantify as a function of Reynolds number. We are able to use our results to describe the hydrodynamic porosity, θ_{mobile} , of the medium because of the direct proportionality between these two quantities.

3.5 The Dead-End Pore Model

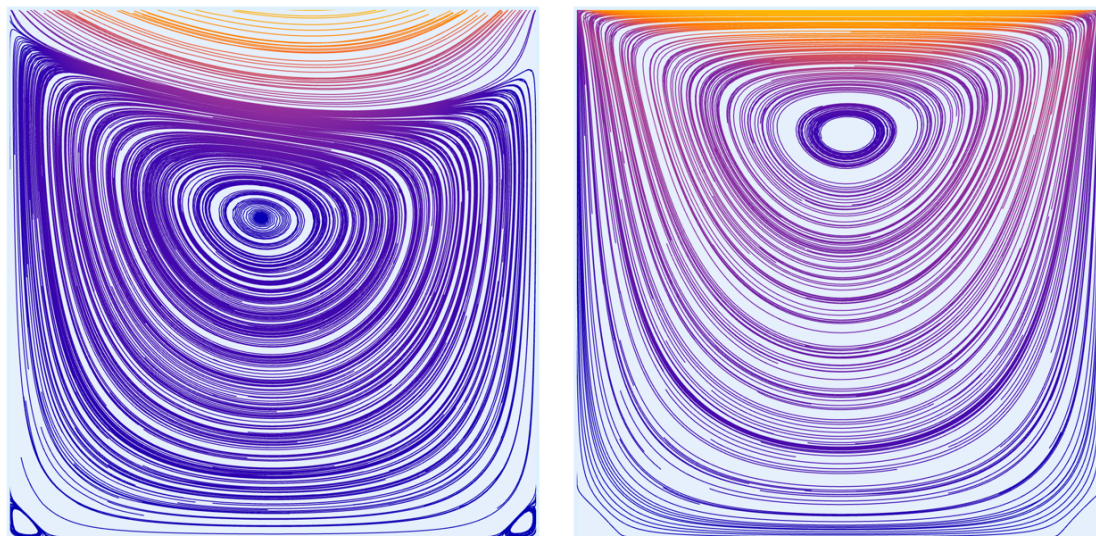
280 If we wished to geometrically simplify the pore space of a porous medium, we would study a single cavity or dead-end pore. The idea of a poorly connected, or dead-end pore was first explored by Turner (1958), who studied channel flow with distributed pockets of stagnant fluid. Although Turner admitted such pore spaces would play a role in diffusion throughout the pore space, other researchers such as Fatt (1959) and Goodknight et al. (1960) initially regarded dead-end pore spaces as regions through which diffusion could not occur. Deans (1963) noted that the division of pore space into flowing and stagnant
285 regions, separated by a “resistance to mass transfer” is an “extreme limit” that can only be justified on the grounds of simplicity. Following this conclusion, Coats and Smith (1964) relaxed the definition of the dead-end pore to account for diffusion, but still referred to the dead-end pore volume as stagnant. Physically, we know this enforcement to be an oversimplification of the recirculatory flow within the dead-end pore space. Chilukuri and Middleman (1984) corrected for this oversimplification by describing mass transport from dead-end pores as a result of vortex-enhanced diffusion – a conclusion that coincides with a
290 series of publications that detail the vortex structures within dead-ended pores (Moffatt, 1963; Mehta and Lavan, 1969; O’ Brien, 1972; Shen and Floryan, 1985; Kang and Chang, 1982; Fang et al., 1997). The evolution of the dead-end pore model is illustrated in Figure 4, below.



295 **Figure 4: Mobile-Immobile Zone model of the dead-end pore space (left), boundary-driven condition, and vortex-enhanced diffusion (middle), shear-driven boundary condition yielding a deformable, mobile separatrix (right).**

Separation of the mobile and immobile zone volumes is described by the boundary- or shear-driven flow models; we refer to the boundary between these zones as the separatrix. In application to flow, the idea of a separatrix was first postured by Elderkin (1975), who describes the boundary as a trajectory that is topologically abnormal in comparison to nearby trajectories. Weiss (1991) later used this concept to describe the defining limit between free and trapped fluid regions. Other publications refer to this boundary as a dividing (Moffatt, 1963; O' Brien, 1972; Higdon, 1985) or separating streamline (Shen and Floryan, 1985; Alkire et al., 1990). The modeling and experimental work on which we build, i.e., Kahler and Kabala (2016, 2018, 2019), and even earlier publications such as Horner et al. (2002), use this same terminology (the separatrix) to describe the fluidic boundary between the mobile and immobile zones in the idealized dead-end pore space.

305 In the case of the boundary-driven model (which is essentially the commonly studied driven-lid problem), the geometric boundary between the mobile and immobile zones also serves as the fixed location of the separatrix. With an increase in Reynolds number of the adjacent through-channel flow, the vortex structures within a cavity translate and smear in the direction of the imposed boundary condition movement. Such results have been illustrated by many and summarized by Shankar and Deshpande (2000). In shear-driven flows, the separatrix is free to move about the cavity space. As discussed by Fang et al. 310 (1999) and Kahler and Kabala (2016), the exact location of the separatrix depends on the Reynolds number of the adjacent through-channel flow in the mobile zone. This means that, unlike in the case of the boundary-driven flow condition, the mobile and immobile zones cannot be defined based on the geometry of the pore space alone. Instead, the volumes of these zones must be defined as flow dependent. In application to square cavity flow, comparison between the enforcement of the boundary-driven and shear-driven flow conditions is provided in Figure 5 below.



315

Figure 5: Vortex location for the mobile and immobile separatrix (left and right, respectively). The location of the mobile separatrix is determined from a shear-driven flow condition. The location of the immobile separatrix is determined from a boundary-driven flow condition. These results are generated for the idealized pore space provided in Figure (4) for $Re = 10$.

In the study of flow past cavities, it is standard practice to enforce the shear-driven boundary condition. Researchers that
320 initially studied these flows, e.g., Moffatt (1963), immediately identified through-flow penetration into the cavity space upon
investigation. O’neill (1977) and Wakiya (1975) found that attachment of the separatrix to the cavity wall occurs at some depth
into the cavity and as Higdon (1985) states, not at the sharp, leading edge of the cavity. In fact, for rectangular cavities
exceeding a given depth ratio, researchers found that the downstream attachment of the separatrix, or dividing streamline,
occurs at the bottom of the cavity wall, mimicking the behavior of a sudden-expansion flow (Shen and Floryan, 1985; Alkire
325 et al., 1990). Enforcement of the boundary-driven flow model would, in this application, yield significant error.

With these findings considered, we again refer to the discussion presented by, Li et al. (1996) wherein the effective porosity
of the studied medium is found to be flow dependent. The authors of this study explain that this dependence is a result of
physical macrostructures that act as preferential flow paths during high flow volumes. What the authors do not discuss, is the
hydrodynamic behavior of the immobile zones within the medium – a behavior that is driven by separatrix movement in to
330 and out of each effectively dead-end pore. As flow volumes increase, the separatrix moves toward its neighboring through-
channel, and the immobile zone it defines grows. The result of an increase in flow volume is a decrease in hydrodynamic
porosity, θ_{mobile} . It is only when the shear-driven flow condition is applied to the dead-end pore that this behavior is observed.
If the mobile and immobile zones are improperly defined by the simplified boundary-driven flow condition, this behavior is
missed.



335 4 Methods

To determine the hydrodynamic porosity, θ_{mobile} , of a porous medium, we study the medium at the pore scale and assume an idealized dead-end pore geometry. The movement of the separatrix is tracked over a range of interstitial Reynolds numbers to determine the relative magnitudes of the mobile and immobile zones, which we then use to calculate the value of the pore-space partitioning coefficient, $\xi = \theta_{mobile}/\theta$.

340 4.1 Numerical Flow Solver

To observe movement of the separatrix in the idealized pore space, we use *Mathematica*'s numerical differential equation solver, *NDSolve*, to solve the continuity equation (mass conservation), Navier-Stokes equations (momentum evolution), and associated boundary conditions. The solver domain is a replica of the idealized pore space utilized by Kahler and Kabala (2016) and is similar in geometry to the domain commonly used in the study of flow past cavities (Chilukuri and Middleman, 1984; Higdon, 1985; Fang et al., 1997). For the sake of simplicity, the flow is modeled as being two-dimensional. The height of the through-channel is the same as the depth and width of the dead-end pore (i.e., the dead-end pore has a depth ratio of 1:1). In the study of flow past cavities, this geometry is by far the most prevalent, as noted by Shankar and Deshpande (2000). The through-channel is extended past the dead-ended pore by twice the channel height to eliminate any end effects associated with the outflow boundary condition. Finally, the dead-ended pore is located one-fourth of the way into the through-channel given the need to input a fully developed flow profile at the through-channel inlet. To exaggerate the movement of the separatrix as a function of Reynolds number, the solver domain is manipulated such that the through-channel becomes much narrower than the depth and width of the cavity space.

The idealized flow geometry is discretized through use of the *ElementMesh* function, which, by default, generates a second-order, triangular element mesh. The interior and boundary mesh elements are further refined by specifying upper limits on the *MaxCellMeasure* and *MaxBoundaryCellMeasure*. A brief convergence analysis of the interior and boundary mesh cell sizes is provided in the supplemental material. Further, a refinement region is specified at the geometric boundary of the channel-cavity interface to ensure proper resolution of the separatrix.

The solver itself is defined by the system of equations that describe steady-state flow through the idealized pore space (i.e., the incompressible form of the continuity and Navier-Stokes equations), as well as the boundary conditions that are assigned to the solver domain. These equations are normalized by the channel height, h , and the average inlet flow velocity, U . The flow is assumed to be steady-state and restricted to the laminar flow regime. A set of Dirichlet conditions are applied to the boundaries of the solver domain (i.e., the no-slip condition at the domain walls and a uniform pressure condition, wherein the pressure is arbitrarily set to zero, at the domain outlet). The inlet velocity profile is defined by the Hagen-Poiseuille model for



fully developed channel flow. Finally, flow is assigned to the entire idealized pore space given that the application of this work is to fully saturated porous media. The properties of water at standard conditions are assigned to the fluid.

Here it is important to note that the non-dimensional form of the Navier Stokes equations is used in this analysis. The scaling on the pressure term is appropriate for flows that are dominated by convective action (i.e., flows in which viscous effects are relatively negligible). This choice was made to replicate the scaling utilized by Kahler and Kabala (2016), who studied flows with channel-based Reynolds numbers of 0.01–10. Fang et al. (1997) used the same scaling, though for admittedly higher channel-based Reynolds numbers in the range of 50–1,600. For our case, and the work on which we build, this scaling is justified because these studies aim to capture flow phenomena driven by convective action (i.e., changes in momentum to the bulk flow). When the Reynolds number approaches 0, and the flow can be approximated as creeping, the scaling on the pressure term can be achieved through use of the flow viscosity.

For this system of equations, *NDSolve* utilizes Finite Element Method to arrive at a solution. In general, the solver method utilized by *NDSolve* is automatically determined by the results of symbolic analysis. The use of Finite Element Method is triggered by specific user inputs. For example, specification of the Navier-Stokes equation using the ‘Inactive’ operator or boundary conditions defined by the *DirichletCondition* function prompt the use of this solver method. Implementation of this solver method can be verified by validating that the solution contains an *ElementMesh* (Wolfram, 2022). The outputs of the solver are three interpolating functions that describe the pressure and velocity fields within the flow domain. Streamlines are visualized through use of the built-in *StreamPlot* command. The error associated with each solver output is determined by the solver mesh (i.e., domain discretization), assigned working precision, and solver method.

4.2 Data Collection

In this work, we vary the Reynolds number of the through-channel flow (i.e., the flow in the mobile zone), and the depth ratio of the idealized dead-end channel-cavity geometry. As noted by Fang (2003), and other publications, the location of the separatrix is a function of both Reynolds number and geometry (Mehta and Lavan, 1969; O’ Brien, 1972; Higdon, 1985; Kim, 2006).

4.2.1 Reynolds Numbers

Below a Reynolds number of 1, the separatrix remains stationary (Kahler and Kabala, 2016). Flows of this nature are classified by the creeping flow regime, where viscous effects dominate. It is not until we study Reynolds numbers within the inertial flow regime that we observe a mobile separatrix. This is because the location of the separatrix is dictated by the inertia of the adjacent through-flow. For this reason, we impose the following Reynolds number, Re , ranges to the through-flow:

- $Re = 0.01 - 1$
(to verify the stationary nature of the separatrix in the creeping flow regime)



- $Re = 1 - 100$

(to illustrate the mobility of the separatrix in the laminar flow regime)

400 To remain within the laminar flow regime, we limit our Reynolds number to a maximum of 100. This choice is admittedly arbitrary, given that transition to turbulence in pipe flow typically occurs over a diameter-based Reynolds number of 2,000 and at least one order of magnitude above the particle-based Reynolds number at which the deviation from Darcy's Law occurs in porous media (Bear, 1975); deviation from Darcy's Law generally occurs between a particle-based Reynolds number of 1 and 10.

405

In terms of particle-based Reynolds numbers, there is ample evidence that the onset of transitional behavior occurs around 100. For columns of packed spheres, Jolls and Hanratty (1966) report the onset of transitional behavior within the range of 110 – 150. Wegner et al. (1971) found a slightly lower range of 90 – 120 for beds of packed spheres. Latifi et al. (1989) encountered transitional behavior at 110, also for a bed of packed spheres; however, the authors did note unsteady laminar
410 flow behavior until 370. A similar study conducted by Rode et al. (1994) reports transitional behavior in the range of 110 – 150. Finally, Bu et al. (2014) define a critical particle-based Reynolds number of 100 as the cutoff for laminar flow, with the onset of turbulence occurring between 230 – 400.

If we instead consider the interstitial Reynolds number, which is based on average pore size and average pore-scale flow
415 velocity, we encounter the commonly cited Reynolds number ranges provided by Dybbs and Edwards (1984), summarized in Table 1 below.

Table 1: Reynolds number ranges corresponding to pre-turbulent flow regimes, as provided by Dybbs and Edwards (1984).

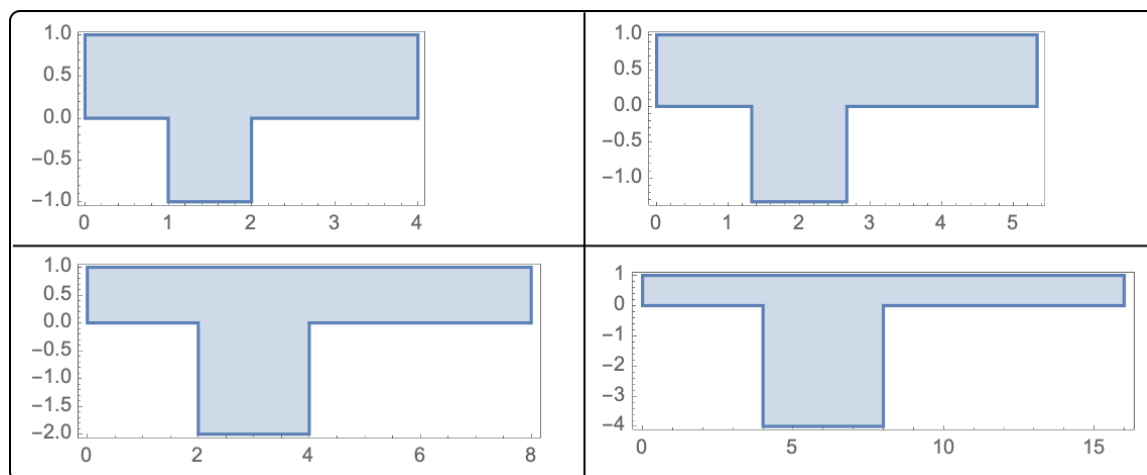
Flow Regime	Reynolds Number Range
Creeping/Darcy	0 – 1
Inertial	1 – 10
Laminar, non-linear	10 – 150
Laminar, unsteady	150 – 300

We can easily imagine representing our system in terms of the interstitial Reynolds number. Given our assumption that the
420 medium is homogeneous, we know the average pore size. Pore-scale flow velocity is typically calculated by dividing the flux through the medium by the porosity of the medium, but in our case, we will impose it directly by assigning a mean velocity to the through-channel flow. Capping our Reynolds number at a value of 100 keeps our analysis within the steady laminar flow regime.



4.2.2 Flow Geometries

425 The effect of pore geometry manipulation has been extensively studied in the literature. In these studies, the authors vary the
type of cavity (i.e., rectangular, circular, etc.), the depth ratio of the cavity, and the size of the cavity relative to the size of the
adjacent through-channel. To replicate the results obtained by Kahler and Kabala (2016), we use an idealized geometry wherein
the height of the through-channel is equivalent to the depth and width of the cavity geometry, as provided in the top-left
quadrant of Figure 6. To exaggerate the mobility of the separatrix in the laminar flow regime, the depth and width of the cavity,
430 relative to the through-channel, are equally increased in magnitude. These geometries are provided in Figure 6, below, and
referred to by channel-cavity depth ratios (i.e., 1:1, 3:4, 1:2, and 1:4). For example, the depth ratio 1:2 corresponds to the
geometry in which the cavity depth and width are twice that of the through-channel height.



435 **Figure 6: Study geometries 1:1 3:4, 1:2, and 1:4; specified by their depth ratio (i.e., channel height to cavity depth/width) in non-dimensional space.**

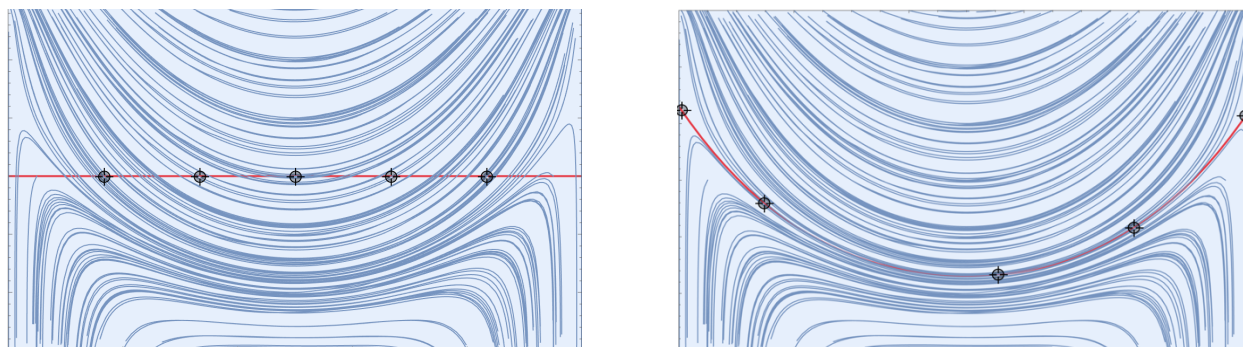
4.3 Measurement Method

To determine the value of the pore-space partitioning coefficient, $\xi = \theta_{mobile}/\theta$, and therefore the hydrodynamic porosity, θ_{mobile} , for each inlet flow condition, we use the following procedure:

1. Generate a monochromatic stream plot of the flow,
- 440 2. Draw the separatrix in the area between the bulk flow in the through-channel and the recirculatory flow in the dead-end pore space in a contrasting color, using the streamlines in the stream plot for guidance,
3. Use an interpolating function to mathematically describe the location of the separatrix,
4. Define the area below the separatrix as the immobile zone, and the area above as the mobile zone and use numerical integration to quantify the magnitude of these regions.



445 To draw the separatrix, we use a *DynamicModule* in *Mathematica* to generate an interpolating function that includes five points (or more) of our choosing between the mobile and immobile zones. This process is pictured below in Figure 7. To determine the sizes of the mobile and immobile zones, we apply numerical integration to the resulting interpolating function.



450 **Figure 7:** A *DynamicModule* automatically places five points on a monochromatic stream plot in the vicinity of the separatrix(left). Given user input (i.e., movement of these five points to the approximate location of the separatrix), the *DynamicModule* produces an interpolating function that can be used to describe the location of the separatrix (right).

Given that the shape and location of this interpolating function are a direct result of user input, there is an inherent error built into the measurement process that we are unable to precisely quantify. Additional errors in the measurement process result from the chosen resolution of the stream plots which is in turn limited by the quality of the solver mesh and working precision
455 assigned to the numerical solver method.

5 Results

5.1 Separatrix Movement

Because the cavity flow is driven by the adjacent through-channel flow, we start by providing a stream plot of the entire dead-end pore geometry adjacent to the corresponding cavity flow in Figure 8. We then provide stream plots for each cavity
460 geometry at Reynolds numbers of 1, 10, 50, and 100 in Figure 9.

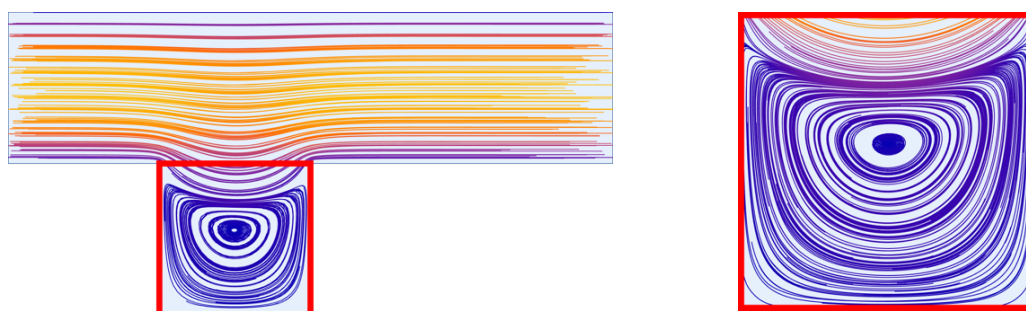
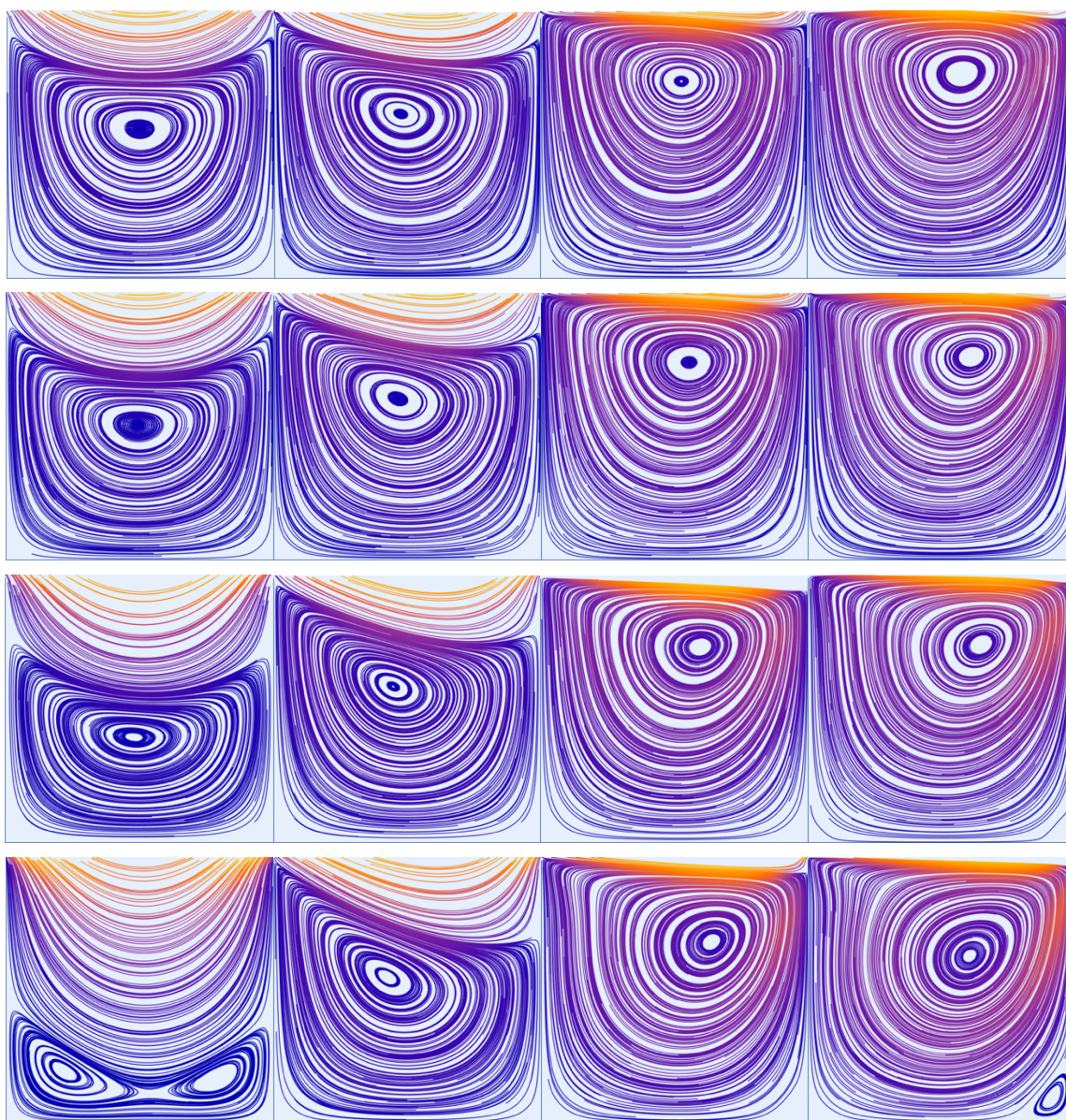


Figure 8: Stream plot magnification example.

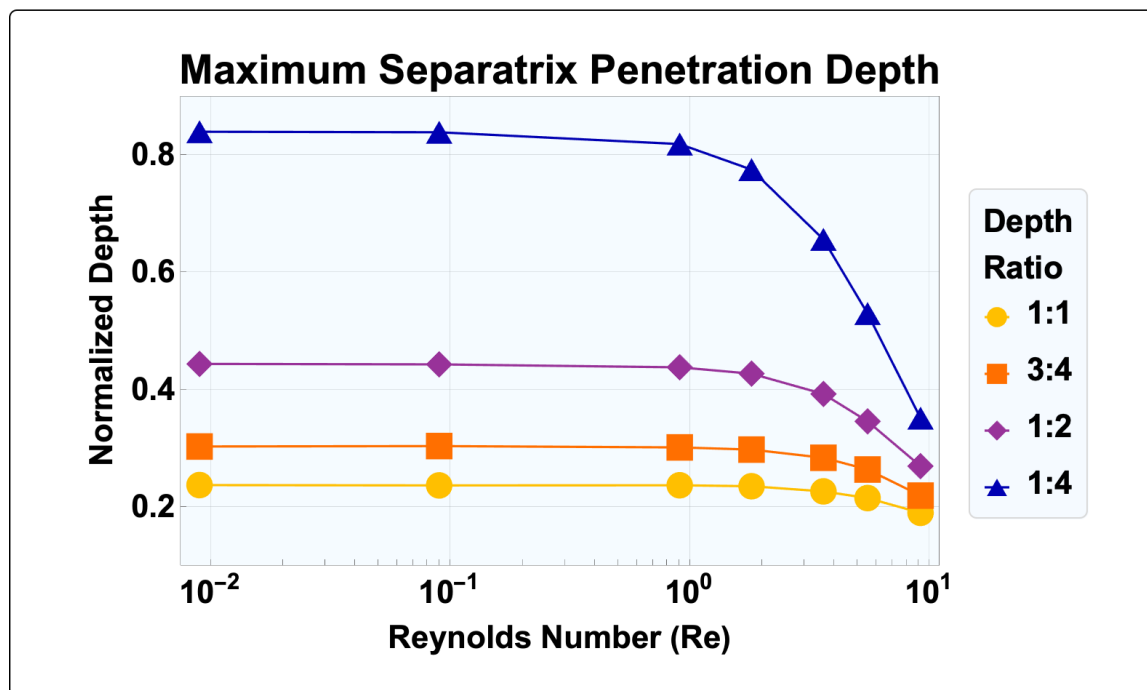


465

Figure 9: Dead-end pore stream plots for each depth ratio (1:1, 3:4, 1:2, and 1:4 from top to bottom) for Reynolds numbers (1, 10, 50, and 100 from left to right).

Movement of the separatrix as a function of Reynolds number was first explored by Kahler and Kabala (2016). In their work, the authors track the bottom-most point of the separatrix to determine its maximum penetration depth into the dead-end pore. To confirm the numerical accuracy of the results produced in this work, we replicate this plot, which is provided in the supplemental material. We expand upon this plot by tracking the movement of the separatrix for three additional flow geometries, as pictured below.

470



475 **Figure 10:** Maximum relative penetration depth of the separatrix into the dead-end pore space as a function of Reynolds number, *Re*.

The results obtained by Kahler and Kabala (2016) reveal an immobile separatrix in the creeping flow regime (i.e., $Re < 1$), and a mobile separatrix in the inertial flow regime. In the former, the bottom-most point of the separatrix does not exceed 25% of the depth of the idealized pore space. Our results replicate the separatrix behavior observed by Kahler and Kabala (2016) and are within, at most, a 2% difference. Over the range of Reynolds numbers plotted in Figure 10, the maximum penetration depth of the separatrix diminishes by 20%.

Building upon the test conditions utilized by Kahler and Kabala (2016), we observe movement of the separatrix toward the geometric boundary of the cavity space for Reynolds numbers approaching 100. Movement of the separatrix within the cavity space is further exaggerated by manipulation of the flow geometry, as illustrated in Figure 11 below.

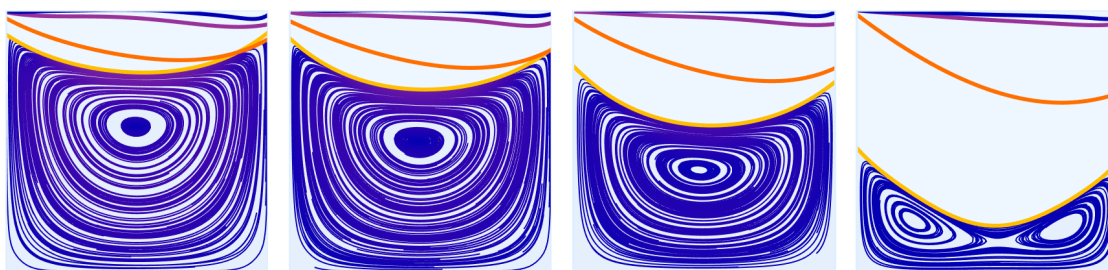


Figure 11: Immobile zone vortex streamlines, corresponding to $Re = 1$, bounded by the separatrix (highlighted in yellow) for each channel-cavity depth ratio, 1:1, 3:4, 1:2, and 1:4 (from left to right). Additional separatrix locations for Reynolds numbers corresponding to 10, 50, and 100 are plotted in orange, purple, and blue, respectively.

490 Movement of the separatrix toward the adjacent through-channel (and out of the cavity space) results in a decrease in the pore-space partitioning coefficient, $\xi = \theta_{mobile}/\theta$, and therefore the hydrodynamic porosity, θ_{mobile} , of the medium. For example, media with cavities described by the dead-end pore model pictured in Figure 4 experience roughly a 4% reduction in θ_{mobile} over the tested Reynolds number range. By comparison, when the channel-cavity depth ratio is 1:4 (i.e., the cavity depth is 4 times that of the through-channel height), θ_{mobile} decreases by approximately 42%. See Table 2 for a summary of the changes

495 associated with each channel-cavity depth ratio; note that given Eq. (10), the provided percent-decrease values are the same for the pore-space partitioning coefficient, ξ , and the hydrodynamic porosity, θ_{mobile} , of the medium.

Table 2: Maximum and minimum pore-space partitioning coefficient, $\xi = \theta_{mobile}/\theta$, values corresponding to an increase in Reynolds number in each tested flow geometry.

Depth Ratio	Pore-Space Partitioning Coefficient, $\xi = \theta_{mobile}/\theta$		
	Max.	Min.	% Decrease
1:1	0.84	0.8	4.34
3:4	0.81	0.75	7.47
1:2	0.79	0.67	15.81
1:4	0.87	0.51	41.50

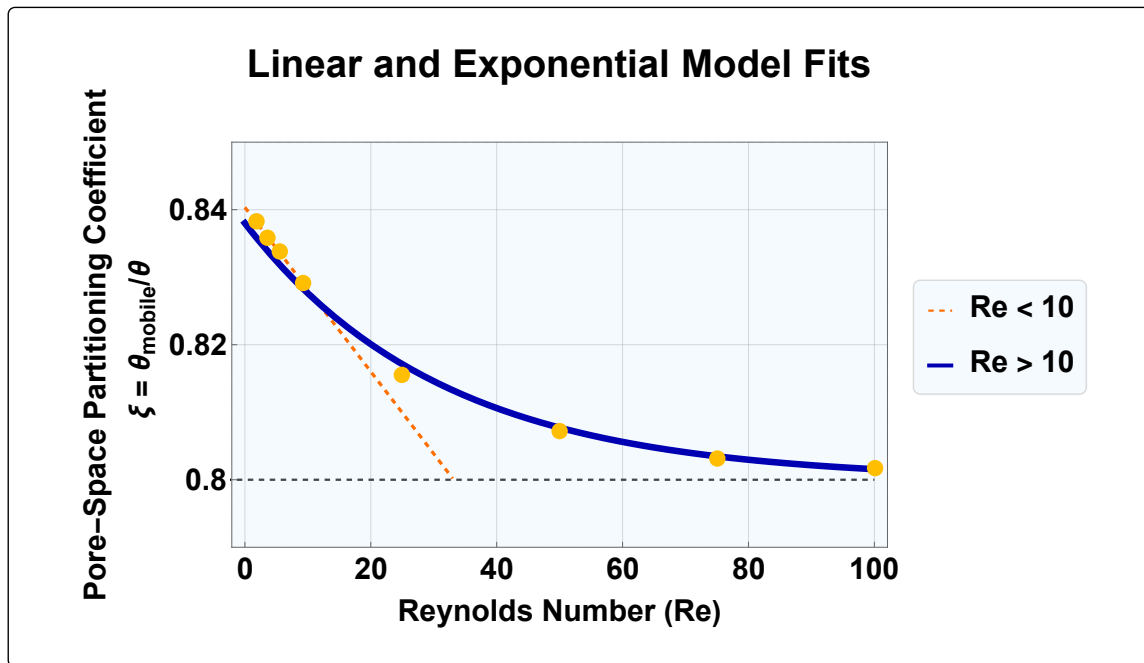
500 5.2 Exponential Dependence of Hydrodynamic Porosity on Pore-Scale Flow Velocity

When plotted, the pore-space partitioning coefficient, $\xi = \theta_{mobile}/\theta$, and therefore the hydrodynamic porosity, θ_{mobile} , of the medium, approaches the value suggested by the boundary-driven model we previously discussed for Reynolds numbers approaching the upper limit of the laminar regime ($Re = 100$). See Figure 12 (below) for evidence of this behavior. In this figure, we also demonstrate that these quantities exhibit a linear dependence on Reynolds number, in the inertial flow regime

505 ($Re = 1 - 10$). Extrapolation of this relationship past $Re = 10$ is provided to illustrate the error that would result from not



utilizing the exponential relationship provided in Eq. (12). Again, we remind readers of the direct proportionality between the partitioning coefficient, $\xi = \theta_{mobile}/\theta$, and the hydrodynamic porosity of the medium, θ_{mobile} .



510 **Figure 12:** The pore-space partitioning coefficient, $\xi = \theta_{mobile}/\theta$, exhibits a linear dependence on Reynolds number, Re , for $Re = 1-10$ and an exponential dependence for $Re = 1-100$. At Reynolds numbers approaching 100, the partitioning coefficient of the flow geometry approaches the value predicted by the boundary-driven flow model. The results pictured here are for the 1:1 channel-cavity depth ratio.

The fit parameters for each channel-cavity depth ratio are provided in Table 3. The quality of each fit is measured by the coefficient of determination (R^2), which is approximately 1 for each tested depth ratio. In the inertial flow regime, the pore-space partitioning coefficient, $\xi = \theta_{mobile}/\theta$, exhibits a linear dependence on Reynolds number. However, as the Reynolds number increases, the partitioning coefficient deviates from this linear model. Instead, a nonlinear dependence on Reynolds number explains the calculated partitioning coefficient values at higher Reynolds numbers, and more significantly, over the entire range of Reynolds numbers, Re , in the laminar regime ($Re = 1-100$). This dependence is well-fit by an exponential function:

520
$$\xi = a + be^{-c v_{pore}} \Leftrightarrow \xi = a + be^{-d Re}, d = \frac{c \text{ height}}{v} \quad (11)$$

This expression can be easily re-written using the help of Eq. (10) to define the hydrodynamic porosity of the medium, θ_{mobile} :

$$\theta_{mobile} = (a + be^{-c v_{pore}}) \theta \Leftrightarrow \theta_{mobile} = (a + be^{-d Re}) \theta \quad (12)$$



Where a is the pore-space partitioning coefficient, $\xi = \theta_{mobile}/\theta$, value approximated by the boundary-driven model (i.e., $Re \rightarrow \infty$), and the quantity ' $a + b$ ' is the value in the creeping flow regime (i.e., $Re \rightarrow 0$). We note that these values, as written, are the same for Eq. (11) and (12).

Table 3: Hydrodynamic porosity, θ_{mobile} , parameters for Reynolds number dependence (d) and pore-flow velocity (c) defined in Eq. (11) and (12).

Depth Ratio	Equation (12) Exponential Fit Parameters				
	R^2	a	b	c (s/m)	d
1:1	1.0000	0.80	3.80×10^{-2}	25.91	3.19×10^{-2}
3:4	1.0000	0.75	6.20×10^{-2}	33.62	4.14×10^{-2}
1:2	1.0000	0.67	1.26×10^{-1}	49.79	6.13×10^{-2}
1:4	0.9993	0.50	3.66×10^{-1}	77.32	9.52×10^{-2}

Mathematically, the fit parameter, b , drives the exponential behavior of our fit. When on the order of magnitude of 10^{-1} the exponential behavior of our fit becomes most exaggerated. This is exemplified in Figure 13, below, for depth ratios 1:4 and 1:2.

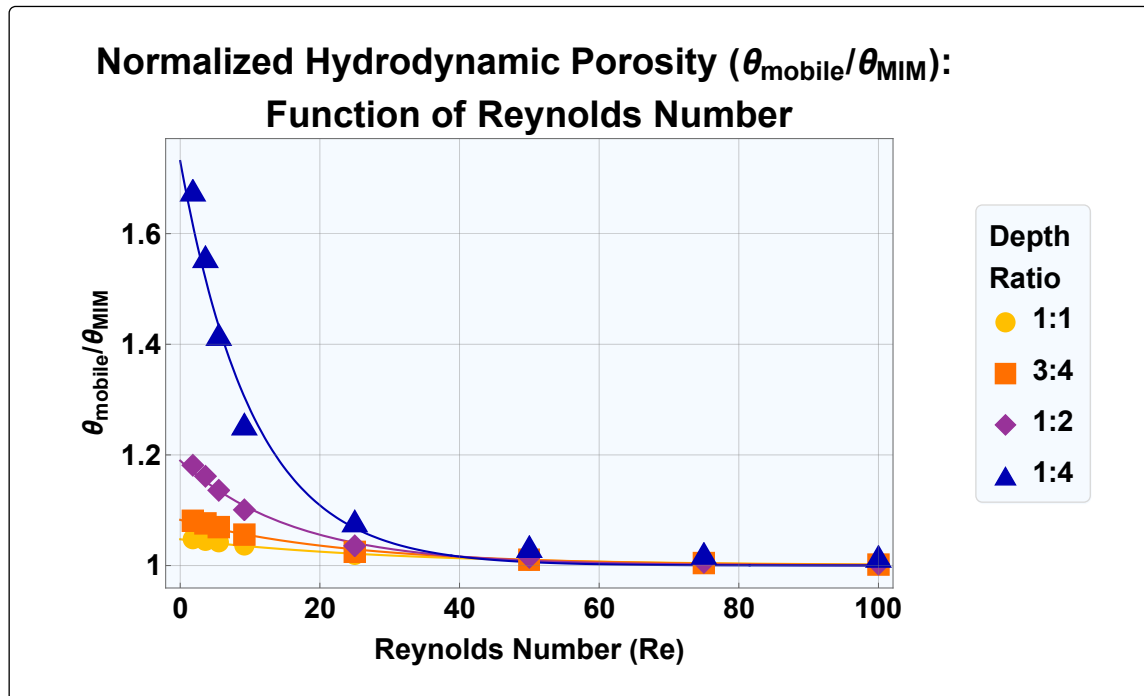


Figure 13: The exponential decay of hydrodynamic porosity, θ_{mobile} , as a function of Reynolds number, Re , for media with cavities of varying channel-cavity depth ratios. For ease of comparison, θ_{mobile} is normalized by the value that corresponds to the Mobile-Immobile Zone model, θ_{MIM} .



In Figure 13, we normalize the hydrodynamic porosity, θ_{mobile} , by the *static* mobile-zone porosity value, θ_{MIM} , that results from enforcement of the Mobile-Immobile Zone model in the dead-end pore space, defined as:

$$\theta_{MIM} = \xi_{MIM} \theta \quad (13)$$

540 The geometric pore-space partitioning coefficient, ξ_{MIM} , is determined by the relative magnitudes of the through-channel and cavity volumes of each dead-end pore geometry. For 1:1 depth ratio pictured in Figure 4, $\xi_{MIM} = 4/5$. For the 1:2 depth ratio pictured in Figure 6, however, $\xi_{MIM} = 8/12$.

6 Calculating Pore-Scale Flow Velocity and Hydrodynamic Porosity Parameters

6.1 Pore-Scale Flow Velocity

We can use this newfound exponential relationship outlined in Eq. (12) to fill in the details of Eq. (5):

545

$$v_{pore} = \frac{v}{(a + b e^{-c v_{pore}}) \theta} \quad (14)$$

Here, we remind readers that v is the volumetric velocity used in Darcy's or Forchheimer-Dupuit's law (Eq. (2) and (3), respectively). To illustrate the ease at which the exponential relationship in Eq. (12) can be incorporated into current models, we provide a brief example utilizing the idealized pore geometry provided in Figure 4, the associated exponential fit coefficients (i.e., $a = 0.80$, $b = 3.80 \times 10^{-2}$, and $c = 25.91$ s/m), and the properties of water assumed by Kahler and Kabala (2016). In this example, we assume the volumetric velocity has a magnitude 10^{-3} (m/s) and a total porosity (θ) of 0.4 – an arbitrary total porosity value in the range typically measured for unconsolidated, unwashed media (i.e., 20 – 45%) (Woessner and Poeter, 2020). Using only 3 Picard iterations with an initial guess of 2×10^{-3} (m/s), we converge to 3 decimal places and a pore-scale flow velocity of 2.99×10^{-3} (m/s). Below, we illustrate the power of *Mathematica*'s built-in *Nest* function, which will, for the same parameter set, converge for an initial guess spanning *twenty orders of magnitude*. In the code provided 555 below, we use the sister, *NestList* function to quickly determine the number of iterations needed for convergence.



? NestList

```
Symbol ⓘ
NestList[f, expr, n] gives a list of the results of applying f to expr 0 through n times.
```

```
vV = 0.001; (*hypothetical volumetric velocity*)
IG = 0.002; (*initial guess*)
vP = NestList[ $\frac{0.001}{n * (a + b * \text{Exp}[-c \#])}$  &, 0.002, 4] (*pore-scale velocity*)
{0.002, 0.00299016, 0.00299344, 0.00299345, 0.00299345}
```

In the table below, we repeat this process for an initial guess 10 orders of magnitude larger and smaller than our original guess to illustrate the robust nature of this method.

Table 4: The pore-scale flow velocity (m/s) can be determined in only a few Picard iterations.

	Pore-Scale Velocity (m/s)			
	Iteration Number			
Initial Guess	1	2	3	4
2×10^{-3}	0.00299016	0.00299344	0.00299345	0.00299345
2×10^{-13}	0.00298329	0.00299342	0.00299345	0.00299345
2×10^7	0.003125	0.00299388	0.00299346	0.00299345

560

From this demonstration, we conclude that implementation of Eq. (12) is no more mathematically burdensome to implement than the constant porosity model, which results in unnecessary error.

6.2 Hydrodynamic Porosity Fit Parameters

In this work, we illustrate how to solve for the exponential fit parameters in Eq. (11) and (12) through numerical simulation. But this is an idealized case – porous media have an array of randomly distributed and sized pore spaces, not to mention drastic changes in pore geometry. If we wanted to use the relationship provided in Eq. (12), we would need to quantify the volumetric and pore-scale flow velocities to then be able to determine the corresponding exponential fit parameters. This could be achieved through column experiments with a known pressure gradient (to solve for the volumetric flow velocity), and a measurable tracer pulse (to solve for the pore-scale flow velocity). Given that Eq. (12) contains three unknown parameters, we would need to conduct this experiment *at least* three times, each at a different, judiciously selected flow condition. To improve fit quality and reduce the effect of measurement noise, we recommend an overdetermined system in practice.

570



575 In this example, we work with an artificial dataset, generated from use of Eq. (14) and the exponential fit parameters we used in our last example (i.e., $a = 0.80$, $b = 3.80 \times 10^{-2}$, and $c = 25.91 \text{ s/m}$). We assume we have measured volumetric velocities that correspond to the laminar flow regime ($Re = 1-100$); for the characteristic height we assign to the dead-end pore geometry (i.e., 0.001 m), the corresponding pore-scale velocity range is approximately 0.001–0.1 (m/s). Let’s assume we measure the volumetric flow velocities 0.01, 0.05, and 0.09 (m/s). Given this assumption, we can calculate the corresponding pore-scale flow velocities:

Table 5: Artificial volumetric and pore-scale flow velocity (m/s) data set, generated from Eq. (13).

Volumetric Velocity (m/s) $\times 10^2$	Pore-Scale Flow Velocity (m/s) $\times 10^2$
1	3.05939
5	15.6122
9	28.1241

580

Moving forward, we assume that we have measured these values experimentally and that we actually do not know the values of our exponential fit parameters, a , b , and c . We can use the synthetic dataset provided in Table 5 to calculate them. This is easily achieved through use of *Mathematica*’s *FindFit* function. Specifying a Newton solution method, we arrive at the anticipated parameter values, *exactly* in 100 iterations (the default value used by the *FindFit* function).

? FindFit

Symbol ?

FindFit[data, expr, pars, vars] finds numerical values of the parameters pars that make expr give a best fit to data as a function of vars.

FindFit[data, {expr, cons}, pars, vars] finds a best fit subject to the parameter constraints cons.

▼

```
vV = {0.01, 0.05, 0.09};
vP = Nest[ $\frac{vV}{n * (a + b * \text{Exp}[-c \#])}$  &, 1, 4];
vData = Transpose[{vP, vV}];
Clear[a, b, c]
FindFit[vData, (n * (a + b * Exp[-c v])) * v, {a, b, c}, v, Method -> "Newton"]
{a -> 0.8, b -> 0.0379998, c -> 25.9902}
```

585

590 Here we note that we have utilized the *arbitrary precision* assigned by *Mathematica* to generate a set of pore-scale velocity values. Realistically, the precision of our measurements would be restricted by our measurement device. Thus, we re-run the above calculation, but this time with only three significant digits rather than the six that we previously used. This time, we arrive at a , b , and c values of 0.801, 0.0366, and 26.4, respectively. The error in our estimated values is 0.09%, 3.65%, and 1.73%. If we increase the precision of our measurements to four significant digits, the error in our estimated values reduces to



0.14%, 0.10%, and 0.25%, respectively. Clearly, accurate estimation of a , b , and c will require numerical fine-tuning and surplus velocity data. This process will need to be conducted via numerical and experimental column tests, which we are currently pursuing.

7 Discussion

595 At scale, the implications of these results are easily observed. For example, consider a periodic medium well-approximated by the dead-end pore model with a measurable total porosity of 0.4. If we assume the non-dimensional idealized pore space pictured in Figure 4, we know that the entire area of the through-channel contributes to the mobile porosity of the medium. The immobile zone is occupied by the vortex, which resides within the dead-end pore. For a Reynolds number of 1, the pore-space partitioning coefficient (ξ) of the dead-end pore geometry is approximately 0.84. Given this value, we can calculate the
 600 hydrodynamic porosity of the medium using Eq. (10):

$$\theta_{mobile} = \xi \theta$$

Resulting, the medium has a hydrodynamic porosity of approximately 0.34. If we had used the boundary-driven flow condition to determine θ_{mobile} (provided in Figures 4 and 5), we would have under-approximated the value at 0.32 by roughly 5%; similarly, we would have over-approximated the immobile porosity by roughly 20%. For the most exaggerated channel-cavity
 605 depth ratio we test (1:4), use of the boundary-driven model would have resulted in a 42% error in θ_{mobile} . This is due to the deep impingement of the through-flow into the dead-end pore for this configuration. We summarize these calculations in the table below:

Table 6: Error in the Mobile-Immobile Zone Model for a Periodic Medium with a Total Porosity of 0.4 and cavity geometry pictured in Figure 4.

	Pore-Space Partitioning Coefficient, $\xi = \theta_{mobile}/\theta$	Mobile Zone Porosity, θ_{mobile}	Immobile Zone Porosity, $\theta_{immobile}$
Hydrodynamic Porosity Model	0.84	0.336	0.064
Mobile-Immobile Zone Model	0.8	0.32	0.08
Mobile-Immobile Zone Model Error (%)		5%	20%

610

Comparing the shear-driven and boundary-driven models, we see that the error in the latter (in terms of the pore-space partitioning coefficient) is largest for flows approaching the creeping flow regime and does not become less than 1 until a Reynolds number of roughly 49 for the channel-cavity depth ratio of 1:1. For the exaggerated flow geometries (i.e., 3:4, 1:2,



and 1:4 depth ratios), the Reynolds number must exceed 51, 48, and 45, respectively. Referring to Figure 5, we see a 17%
615 error associated with the use of the boundary-driven model.

The exponential fit quality is unsurprising. Exponentials play an important role in the solution of differential equations and are
common to groundwater flow modeling. Consider the use of exponential forms in the various renditions of the well function
(e.g., Theis (1935), Hantush (1960), etc.), Gardener's equation for hydraulic conductivity (Gardener, 1958), and even the
620 relationship between soil water content and electrical resistivity (Pozdnyakov et al., 2006). In nature, an exponential decline
in hydraulic conductivity with depth is considered a hallmark of catchment hydrology (Ameli et al., 2016).

Naturally, next steps for this work are in application to groundwater flow models at the macro-scale. The flow geometry
pictured in Figure 4 is an oversimplification of the pore space, meaning that results from this work are purely illustrative of
625 order of magnitude. These results could be made more realistic by establishing the Reynolds number dependence for a more
exhaustive set of flow geometries, and more importantly, geometries that exhibit periodicity. The ability to quantify the
exponential fit parameters at sites needing remediation, as we previously discussed, is also necessary to demonstrate the ease
with which this relationship can be tailored to any given media. We present the results from the former research avenue in our
associated work, *Hydrodynamic Porosity: A Paradigm Shift in Flow and Transport Through Porous Media, Part II*, and are
630 currently pursuing the latter research avenue.

8 Study Limitations

The results of this study are not exact. The location of the separatrix is determined via a stream plot with limited resolution.
From this stream plot, the separatrix location, and ultimately the hydrodynamic porosity, θ_{mobile} , is approximated by a
graphical method that is entirely dependent on user input. However, the repeatability of this measurement process is acceptable
635 – for the idealized pore space pictured in Figure 4 (i.e., a channel-cavity depth ratio of 1:1), and a Reynolds number of 0.01,
the maximum penetration depth of the separatrix was found to vary by 0.005 across 5 measurements. Relative to an average
penetration depth of 0.25, this variation accounts for less than 2% of the magnitude of the mean. Like the values reported in
Section 6, these errors are purely illustrative of order of magnitude. Both quantities are dependent on the consistency of user
input and will also vary between users.

640 Additionally, we consider only the immobile zones generated by dead-end pores and cavity-like structures that generate flow
separation. We do not consider the immobile zones that result from molecular forces between the media and the flowing
solution, nor do we consider surface tension effects. However, we assume that these immobile zones, just as the ones studied
in this work, would behave similarly so long as the Reynolds number of the interstitial flow is appropriate.



645 9 Conclusions

In this work, we explore a physical phenomenon that has been largely neglected in the literature. Generally, the porosity of a medium that is conducive to through-flow, what we define as *hydrodynamic porosity*, θ_{mobile} , is still thought to be a static parameter. Researchers define this quantity using the cumulative volume of the flow through-channels (i.e., mobile zones); cavities and other effectively immobile zones are not considered to significantly contribute to the through-flow volume. We
650 find this approximation to be a notable oversimplification in the creeping and inertial flow regimes, leading to a significant misunderstanding of induced subsurface flows and the accompanying transport processes that determine the efficacy of groundwater remediation projects.

Although a few researchers have previously acknowledged the dependence of what they analogously define as effective
655 porosity on the flow velocity in rock formations, these researchers did not quantify this relationship. In this work, we demonstrate and quantify, explicitly, the dependence of hydrodynamic porosity, θ_{mobile} , on pore-scale flow velocity, for the first time. We begin with a direct replication of the results provided by Kahler and Kabala (2016), wherein the boundaries between the mobile and immobile zones of porous media are shown to be hydrodynamic in nature. We then study the movement of this boundary over a range of interstitial, or channel-based, Reynolds numbers in the laminar flow regime in
660 porous media. The movement of this boundary defines the pore-space partitioning coefficient, $\xi = \theta_{mobile}/\theta$ (i.e., the fraction of the pore space conducive to through-flow), and therefore the hydrodynamic porosity, θ_{mobile} , of the medium. Given the direct proportionality between these quantities, we find both to have an exponential dependence on Reynolds number or pore-scale flow velocity, which we provide in Eq. (11) and (12). Finally, we show that this dependence can be easily incorporated into porous media flow modeling using only a few Picard iterations, even with an initial guess that is over 10 orders of
665 magnitude off.

The flow-dependent nature of hydrodynamic porosity, θ_{mobile} , plays an unmistakable role in the transport of contaminants into and out of immobile zones and is therefore responsible for contributing to phenomena like contaminant rebound after the completion of active remediation strategies (e.g., steady flow pump-and-treat). Researchers who incorporate this phenomenon
670 into their models could better mitigate these transport phenomena with novel strategies, such as rapidly pulsed pump-and-treat remediation.

Data and Code Availability

The simulation data that support the findings of this study, and the corresponding *Mathematica* code files, are available in Open Science Framework at DOI 10.17605/OSF.IO/P2EMN. All files are also provided in pdf format for readers that do not
675 have access to *Mathematica*.



Author Contributions Statement

Conceptualization (Z.J.K.), data curation (A.H.Y.), formal analysis (A.H.Y.), investigation (A.H.Y. and Z.J.K.), methodology (A.H.Y. and Z.J.K.), project administration (Z.J.K.), supervision (Z.J.K.), validation (A.H.Y.), visualization (A.H.Y.), writing – original draft (A.H.Y. and Z.J.K.), writing – review & editing (A.H.Y. and Z.J.K.).

680 Declaration Of Competing Interest

The authors declare no competing conflict of interest.

Acknowledgements

This work is, in part, supported by a grant, OPP1173370 (Sanitation Technology Cluster), from the Bill & Melinda Gates Foundation through Duke University's Center for WaSH-AID. All opinions, findings, and conclusions or recommendations
685 expressed in these works are those of the author(s) and do not necessarily reflect the views of the Foundation, Duke, or the Center.



References

- 690 Alkire, R. C., Deligianni, H., and Ju, J. B.: Effect of Fluid-Flow on Convective-Transport in Small Cavities, *J. Electrochem. Soc.*, 137, 818-824, <https://doi.org/10.1149/1.2086562>, 1990.
- Ameli, A. A., McDonnell, J. J., and Bishop, K.: The Exponential Decline in Saturated Hydraulic Conductivity with Depth: A Novel Method for Exploring Its Effect on Water Flow Paths and Transit Time Distribution, *Hydrol. Process.*, 30, 2438-2450, <https://doi.org/10.1002/hyp.10777>, 2016.
- 695 Arulanantham, R.: Presentation to the Committee on Intrinsic Remediation, Third Meeting, Woods Hole, Mass., June 1 - 2, 1998.
- Bear, J.: *Dynamics of Fluids in Porous Media*, *Soil Sci.*, 120, 162-163, 1975.
- Brutsaert, W.: *Hydrology - an Introduction*, Cambridge University Press, 2005.
- Bu, S., Yang, J., Dong, Q., and Wang, Q.: Experimental Study of Transition Flow in Packed Beds of Spheres with Different Particle Sizes Based on Electrochemical Microelectrodes Measurement, *Appl. Therm. Eng.*, 73, 1525-1532, <https://doi.org/10.1016/j.applthermaleng.2014.03.063>, 2014.
- 700 Cartwright, N., Nielsen, P., and Perrochet, P.: Behavior of a Shallow Water Table under Periodic Flow Conditions, *Water Resour. Res.*, 45, <https://doi.org/10.1029/2008WR007306>, 2009.
- Chen, Y.-F., Zhou, J.-Q., Hu, S.-H., Hu, R., and Zhou, C.-B.: Evaluation of Forchheimer Equation Coefficients for Non-Darcy Flow in Deformable Rough-Walled Fractures, *J. Hydrol.*, 529, 993-1006, <https://doi.org/10.1016/j.jhydrol.2015.09.021>, 2015.
- 705 Chilukuri, R. and Middleman, S.: Cleaning of a Rough Rigid Surface - Removal of a Dissolved Contaminant by Convection-Enhanced Diffusion and Chemical-Reaction, *J. Electrochem. Soc.*, 131, 1169-1173, <https://doi.org/10.1149/1.2115772>, 1984.
- Coats, K. H. and Smith, B. D.: Dead-End Pore Volume and Dispersion in Porous Media, *Soc. Petrol. Eng. J.*, 4, 73-84, <https://doi.org/10.2118/647-pa>, 1964.
- 710 Deans, H. A.: A Mathematical Model for Dispersion in the Direction of Flow in Porous Media, *Soc. Petrol. Eng. J.*, 3, 49-52, <https://doi.org/10.2118/493-pa>, 1963.
- Dinkel, E., Braun, B., Schroder, J., Muhrbeck, M., Reul, W., Meeder, A., Szewzyk, U., and Scheytt, T.: Groundwater Circulation Wells for Geothermal Use and Their Impact on Groundwater Quality, *Geothermics*, 86, <https://doi.org/10.1016/j.geothermics.2020.101812>, 2020.
- 715 Dybbs, A. and Edwards, R. V.: A New Look at Porous Media Fluid Mechanics — Darcy to Turbulent, in: *Fundamentals of Transport Phenomena in Porous Media*, edited by: Bear, J., and Corapcioglu, M. Y., Springer Netherlands, Dordrecht, 199-256, https://doi.org/10.1007/978-94-009-6175-3_4, 1984.
- Elderkin, R. H.: Separatrix Structure for Elliptic Flows, *Am. J. Math.*, 97, 221-247, <https://doi.org/10.2307/2373669>, 1975.
- 720 Ètudes, D. J.: *Thèoriques Et Pratiques Sur Le Mouvement Des Eaux*, Paris, Dunod, 1863.
- Fang, L.-C.: Effect of Mixed Convection on Transient Hydrodynamic Removal of a Contaminant from a Cavity, *Int. J. Heat Mass Tran.*, 46, 2039-2049, [https://doi.org/10.1016/s0017-9310\(02\)00507-0](https://doi.org/10.1016/s0017-9310(02)00507-0), 2003.



- 725 Fang, L. C., Cleaver, J. W., and Nicolaou, D.: Hydrodynamic Cleansing of Cavities, 8th International Conference on Computational Methods and Experimental Measurements (CMEM 97), Rhodes, Greece, May, WOS:A1997BJ12J00038, 391-401, 1997.
- Fang, L. C., Nicolaou, D., and Cleaver, J. W.: Transient Removal of a Contaminated Fluid from a Cavity, *Int. J. Heat Fluid Fl.*, 20, 605-613, [https://doi.org/10.1016/s0142-727x\(99\)00050-8](https://doi.org/10.1016/s0142-727x(99)00050-8), 1999.
- Fatt, I.: Pore Structure of Sintered Glass from Diffusion and Resistance Measurements, *J. Phys. Chem-US*, 63, 751-752, <https://doi.org/10.1021/j150575a031>, 1959.
- 730 Flint, L. E. and Selker, J. S.: Use of Porosity to Estimate Hydraulic Properties of Volcanic Tuffs, *Adv. Water Resour.*, 26, 561-571, [https://doi.org/10.1016/S0309-1708\(02\)00182-3](https://doi.org/10.1016/S0309-1708(02)00182-3), 2003.
- Forchheimer, P.: *Wasserbewegung Durch Boden Zeit*, Vol. 45, Ver. Deut. Ing, 1901.
- Gardener, W. R.: Some Steady-State Solutions of the Unsaturated Moisture Flow Equation with Application to Evaporation from a Water Table, *Soil Sci.*, 85, 228-232, 1958.
- 735 Goodknight, R. C., Klikoff, W. A., and Fatt, I.: Non-Steady-State Fluid Flow and Diffusion in Porous Media Containing Dead-End Pore Volume, *J. Phys. Chem-US*, 64, 1162-1168, <https://doi.org/10.1021/j100838a014>, 1960.
- Hadley, P. W. and Newell, C. J.: Groundwater Remediation: The Next 30 Years, *Groundwater*, 50, 669-678, <https://doi.org/10.1111/j.1745-6584.2012.00942.x>, 2012.
- 740 Hantush, M. S.: Modification of the Theory of Leaky Aquifers, *J. Geophys. Res.*, 65, 3713-3725, <https://doi.org/10.1029/JZ065i011p03713>, 1960.
- Hapgood, K. P., Litster, J. D., Biggs, S. R., and Howes, T.: Drop Penetration into Porous Powder Beds, *J. Colloid Interf. Sci.*, 253, 353-366, <https://doi.org/10.1006/jcis.2002.8527>, 2002.
- Helalia, A. M.: The Relation between Soil Infiltration and Effective Porosity in Different Soils, *Agr. Water Manage.*, 24, 39-47, [https://doi.org/10.1016/0378-3774\(93\)90060-N](https://doi.org/10.1016/0378-3774(93)90060-N), 1993.
- 745 Higdon, J. J. L.: Stokes Flow in Arbitrary Two-Dimensional Domains: Shear Flow over Ridges and Cavities, *J. Fluid Mech.*, 159, <https://doi.org/10.1017/s0022112085003172>, 1985.
- Horner, M., Metcalfe, G. U. Y., Wiggins, S., and Ottino, J. M.: Transport Enhancement Mechanisms in Open Cavities, *J. Fluid Mech.*, 452, 199-229, <https://doi.org/10.1017/s0022112001006917>, 2002.
- 750 Howes, T. and Shardlow, P. J.: Simulation of Mixing in Unsteady Flow through a Periodically Obstructed Channel, *Chem. Eng. Sci.*, 52, 1215-1225, [https://doi.org/10.1016/s0009-2509\(96\)00361-2](https://doi.org/10.1016/s0009-2509(96)00361-2), 1997.
- Jacombs, A. S. W., Karatassas, A., Klosterhalfen, B., Richter, K., Patiniott, P., and Hensman, C.: Biofilms and Effective Porosity of Hernia Mesh: Are They Silent Assassins?, *Hernia*, 24, 197-204, <https://doi.org/10.1007/s10029-019-02063-y>, 2020.
- 755 Jana, S. C. and Ottino, J. M.: Chaos-Enhanced Transport in Cellular Flows, *Philos. T. Roy. Soc. A.*, 338, 519-532, <https://doi.org/10.1098/rsta.1992.0018>, 1992.



- Jolls, K. R. and Hanratty, T. J.: Transition to Turbulence for Flow through a Dumped Bed of Spheres, *Chem. Eng. Sci.*, 21, 1185-&, [https://doi.org/10.1016/0009-2509\(66\)85038-8](https://doi.org/10.1016/0009-2509(66)85038-8), 1966.
- Kabala, Z. J.: The Dipole Flow Test - a New Single-Borehole Test for Aquifer Characterization, *Water Resour. Res.*, 29, 99-107, <https://doi.org/10.1029/92wr01820>, 1993.
- 760 Kabala, Z. J. and Kim, Y.-W.: Dynamic Effective Porosity: Numerical Simulations, *The Journal of Research Institute for Engineering and Technology*, 30, 91-95, 2011.
- Kabala, Z. J. and Xiang, J.: Skin Effect and Its Elimination for Single-Borehole Aquifer Tests, 9th International Conf on Computational Methods in Water Resources, Univ Colorado, Denver, Co, Jun, WOS:A1992BW28Z00051, 467-474, 1992.
- 765 Kahler, D. M. and Kabala, Z. J.: Acceleration of Groundwater Remediation by Deep Sweeps and Vortex Ejections Induced by Rapidly Pulsed Pumping, *Water Resour. Res.*, 52, 3930-3940, <https://doi.org/10.1002/2015wr017157>, 2016.
- Kahler, D. M. and Kabala, Z. J.: Rapidly Pulsed Pumping Accelerates Remediation in a Vertical Circulation Well Model, *Water*, 10, <https://doi.org/10.3390/w10101423>, 2018.
- Kahler, D. M. and Kabala, Z. J.: Acceleration of Groundwater Remediation by Rapidly Pulsed Pumping: Laboratory Column Tests, *J. Environ. Eng.*, 145, [https://doi.org/10.1061/\(asce\)je.1943-7870.0001479](https://doi.org/10.1061/(asce)je.1943-7870.0001479), 2019.
- 770 Kang, I. S. and Chang, H. N.: The Effect of Turbulence Promoters on Mass-Transfer - Numerical-Analysis and Flow Visualization, *Int. J. Heat Mass Tran.*, 25, 1167-1181, [https://doi.org/10.1016/0017-9310\(82\)90211-3](https://doi.org/10.1016/0017-9310(82)90211-3), 1982.
- Kim, Y.-W.: Pore-Scale Flow and Contaminant Transport in Porous Media, Dissertation, Civil and Environmental Engineering, Duke University, Durham, NC, 183 pp., 2006.
- 775 Kwaw, A. K., Dou, Z., Wang, J., Zhang, X., and Chen, Y.: Advancing the Knowledge of Solute Transport in the Presence of Bound Water in Mixed Porous Media Based on Low-Field Nuclear Magnetic Resonance, *J. Hydrol.*, 617, 129059, <https://doi.org/10.1016/j.jhydrol.2023.129059>, 2023.
- Latifi, M. A., Midoux, N., Storck, A., and Gence, J. N.: The Use of Micro-Electrodes in the Study of the Flow Regimes in a Packed-Bed Reactor with Single-Phase Liquid Flow, *Chem. Eng. Sci.*, 44, 2501-2508, [https://doi.org/10.1016/0009-2509\(89\)85194-2](https://doi.org/10.1016/0009-2509(89)85194-2), 1989.
- 780 Li, H., Ohtsuka, Y., Mori, N., Inagaki, T., and Misawa, S.: Effective Porosity and Specific Yield of a Sedimentary Rock Determined by a Field Tracing Test Using Tritium as a Tracer, *Environ. Geol.*, 27, 170-177, 1996.
- Li, X., Wen, Z., Zhan, H., Zhu, Q., and Jakada, H.: On the Bimodal Radial Solute Transport in Dual-Permeability Porous Media, *Water Resour. Res.*, 58, e2022WR032580, <https://doi.org/10.1029/2022WR032580>, 2022.
- 785 Lindsay, J. D.: Relative Flow Porosity in Fibrous Media - Measurements and Analysis, Including Dispersion Effects, *Tappi J.*, 77, 225-239, 1994.
- Luo, Z., Kong, J., Yao, L., Lu, C., Li, L., and Barry, D. A.: Dynamic Effective Porosity Explains Laboratory Experiments on Water Table Fluctuations in Coastal Unconfined Aquifers, *Adv. Water Resour.*, 171, 104354, <https://doi.org/10.1016/j.advwatres.2022.104354>, 2023.
- 790 Ma, C., Shi, W., and Zhan, H.: On the Vertical Circulation Wells in a Leaky-Confined Aquifer, *J. Hydrol.*, 608, 127676, <https://doi.org/10.1016/j.jhydrol.2022.127676>, 2022.



- McCarty, P. L.: Ground Water and Soil Contamination Remediation: Toward Compatible Science, Policy, and Public Perception, The National Academies Press, Washington, DC, 273 pp., <https://doi.org/10.17226/20303>, 1990.
- McDonald, P. J., Istok, O., Janota, M., Gajewicz-Jaromin, A. M., and Faux, D. A.: Sorption, Anomalous Water Transport and Dynamic Porosity in Cement Paste: A Spatially Localised 1h Nmr Relaxation Study and a Proposed Mechanism, Cement Concrete Res., 133, 106045, <https://doi.org/10.1016/j.cemconres.2020.106045>, 2020.
- 795
- Mehta, U. B. and Lavan, Z.: Flow in a Two-Dimensional Channel with a Rectangular Cavity, J. Appl. Mech., 36, 897, <https://doi.org/10.1115/1.3564799>, 1969.
- Moffatt, H. K.: Viscous and Resistive Eddies near a Sharp Corner, J. Fluid Mech., 18, 1-18, <https://doi.org/10.1017/s0022112064000015>, 1963.
- 800
- Muljadi, B. P., Blunt, M. J., Raeini, A. Q., and Bijeljic, B.: The Impact of Porous Media Heterogeneity on Non-Darcy Flow Behaviour from Pore-Scale Simulation, Adv. Water Resour., 95, 329-340, <https://doi.org/10.1016/j.advwatres.2015.05.019>, 2016.
- National Research Council: Natural Attenuation for Groundwater Remediation, The National Academies Press, Washington, DC, 288 pp., <https://doi.org/10.17226/9792>, 2000.
- 805
- Newell, C. J., Adamson, D. T., Kulkarni, P. R., Nzeribe, B. N., Connor, J. A., Popovic, J., and Stroo, H. F.: Monitored Natural Attenuation to Manage Pfas Impacts to Groundwater: Potential Guidelines, Remediation-the Journal of Environmental Cleanup Costs Technologies & Techniques, 31, 7-17, <https://doi.org/10.1002/rem.21697>, 2021.
- O' Brien, V.: Closed Streamlines Associated with Channel Flow over a Cavity, Phys. Fluids, 15, <https://doi.org/10.1063/1.1693840>, 1972.
- 810
- O'Neill, M. E.: Separation of a Slow Linear Shear-Flow from a Cylindrical Ridge or Trough in a Plane, Z. Angew. Math Phys., 28, 439-448, <https://doi.org/10.1007/bf01601625>, 1977.
- Soil & Groundwater Remediation: <https://www.energy.gov/em/soil-groundwater-remediation>, last access: June 1, 2023.
- Fy24 Budget Request: <https://www.energy.gov/em/office-environmental-management>, last access: June 1, 2023.
- Philip, R. D. and Walter, G. R.: Prediction of Flow and Hydraulic-Head Fields for Vertical Circulation Wells, Groundwater, 30, 765-773, <https://doi.org/10.1111/j.1745-6584.1992.tb01562.x>, 1992.
- 815
- Powers, M. B., and D. K. Rubin: Doing What Comes Naturally—Nothing, Engineering News-Record, 16-28, 1996.
- Pozdnyakov, A. I., Pozdnyakova, L. A., and Karpachevskii, L. O.: Relationship between Water Tension and Electrical Resistivity in Soils, Eurasian Soil Sci+, 39, S78-S83, <https://doi.org/10.1134/S1064229306130138>, 2006.
- Qiu, J.: Environmental Science China to Spend Billions Cleaning up Groundwater, Science, 334, 745-745, <https://doi.org/10.1126/science.334.6057.745>, 2011.
- 820
- Rode, S., Midoux, N., Latifi, M. A., Storck, A., and Saadjian, E.: Hydrodynamics of Liquid Flow in Packed Beds: An Experimental Study Using Electrochemical Shear Rate Sensors, Chem. Eng. Sci., 49, 889-900, [https://doi.org/10.1016/0009-2509\(94\)80025-1](https://doi.org/10.1016/0009-2509(94)80025-1), 1994.



- 825 Russell, M., Colglazier, E. W., and English, M. R.: Hazardous Waste Remediation: The Task Ahead, University of Tennessee, Waste Management Research and Education Institute, 1991.
- Sevee, J. E.: Effective Porosity Measurement of a Marine Clay, *J. Environ. Eng.*, 136, 674-681, <https://doi.org/10.1061/%28ASCE%29EE.1943-7870.0000205>, 2010.
- Shankar, P. N. and Deshpande, M. D.: Fluid Mechanics in the Driven Cavity, *Annu. Rev. Fluid Mech.*, 32, 93-136, <https://doi.org/10.1146/annurev.fluid.32.1.93>, 2000.
- 830 Shen, C. and Floryan, J. M.: Low Reynolds Number Flow over Cavities, *Phys. Fluids*, 28, <https://doi.org/10.1063/1.865366>, 1985.
- Sheng, G., Javadpour, F., and Su, Y.: Dynamic Porosity and Apparent Permeability in Porous Organic Matter of Shale Gas Reservoirs, *Fuel*, 251, 341-351, <https://doi.org/10.1016/j.fuel.2019.04.044>, 2019.
- 835 Sutton, D. J., Kabala, Z. J., Schaad, D. E., and Ruud, N. C.: The Dipole-Flow Test with a Tracer: A New Single-Borehole Tracer Test for Aquifer Characterization, *J. Contam. Hydrol.*, 44, 71-101, [https://doi.org/10.1016/S0169-7722\(00\)00083-8](https://doi.org/10.1016/S0169-7722(00)00083-8), 2000.
- Groundwater: Our Most Valuable Hidden Resource: <https://www.nature.org/en-us/what-we-do/our-insights/perspectives/groundwater-most-valuable-resource/>, last access: June 1, 2023.
- 840 Theis, C. V.: The Relation between the Lowering of the Piezometric Surface and the Rate and Duration of Discharge of a Well Using Ground-Water Storage, *Eos, Transactions American Geophysical Union*, 16, 519-524, <https://doi.org/10.1029/TR016i002p00519>, 1935.
- Thomson, N. R., Roos, G. N., Wilson, R. D., Thornton, S. F., and Tolson, B.: The Dipole Flow and Reactive Tracer Test for Aquifer Parameter Estimation, 61st Canadian Geotechnical Conference and the 9th Joint CGS/IAH-CNC Groundwater Conference, Alberta, Canada, 2008.
- 845 Timlin, D. J., Ahuja, L. R., Pachepsky, Y., Williams, R. D., Gimenez, D., and Rawls, W.: Use of Brooks-Corey Parameters to Improve Estimates of Saturated Conductivity from Effective Porosity, *Soil Sci. Soc. Am. J.*, 63, 1086-1092, <https://doi.org/10.2136/sssaj1999.6351086x>, 1999.
- Toyama, K., Togi, F., and Harada, S.: Mass Transfer from Mobile to Immobile Regions in Irregularly Shaped Micro-Channels at Low Reynolds Number, *Groundwater*, <https://doi.org/10.1111/gwat.13276>, 2022.
- 850 Truex, M., Johnson, C., Macbeth, T., Becker, D., Lynch, K., Giaudrone, D., Frantz, Aaron, and Lee, H.: Performance Assessment of Pump-and-Treat Systems, *Groundwater Monitoring & Remediation*, 37, 28-44, <https://doi.org/10.1111/gwmr.12218>, 2017.
- Turner, G. A.: The Flow-Structure in Packed Beds - a Theoretical Investigation Utilizing Frequency Response, *Chem. Eng. Sci.*, 7, 156-165, [https://doi.org/10.1016/0009-2509\(58\)80022-6](https://doi.org/10.1016/0009-2509(58)80022-6), 1958.
- 855 Superfund: National Priorities List (Npl): <https://www.epa.gov/superfund/superfund-national-priorities-list-npl>, last
- Vangenuchten, M. T. and Wierenga, P. J.: Mass-Transfer Studies in Sorbing Porous-Media .1. Analytical Solutions, *Soil Sci. Soc. Am. J.*, 40, 473-480, <https://doi.org/10.2136/sssaj1976.03615995004000040011x>, 1976.



- Wakiya, S.: Application of Bipolar Coordinates to 2-Dimensional Creeping Motion of a Liquid .3. Separation in Stokes Flows, *J. Phys. Soc. Jpn.*, 45, 1756-1763, <https://doi.org/10.1143/jpsj.45.1756>, 1975.
- 860 Wegner, T. H., Karabelas, A. J., and Hanratty, T. J.: Visual Studies of Flow in a Regular Array of Spheres, *Chem. Eng. Sci.*, 26, [https://doi.org/10.1016/0009-2509\(71\)86081-5](https://doi.org/10.1016/0009-2509(71)86081-5), 1971.
- Weiss, J. B.: Transport and Mixing in Traveling Waves, *Phys. Fluids A-Fluid.*, 3, 1379-1384, <https://doi.org/10.1063/1.858068>, 1991.
- 865 Werth, A. J.: Flow-Dependent Porosity and Other Biomechanical Properties of Mysticete Baleen, *J. Exp. Biol.*, 216, 1152-1159, <https://doi.org/10.1242/jeb.078931>, 2013.
- Woessner, W. W. and Poeter, E. P.: Total Porosity, in: *Hydrogeologic Properties of Earth Materials and Principles of Groundwater Flow*, Groundwater Project, Guelph, Ontario, Canada, 2020.
- Finite Element Method User Guide:
<https://reference.wolfram.com/language/FEMDocumentation/tutorial/FiniteElementOverview.html>, last access: June 1, 2023.
- 870 Xia, Q., Zhang, Q., Xu, M., Tang, Y. G., and Teng, H. W.: Visualizing Hydraulic Zones of a Vertical Circulation Well in Presence of Ambient Flow, *Desalin. Water Treat.*, 159, 151-160, <https://doi.org/10.5004/dwt.2019.24098>, 2019.
- Zhou, L., Lassabatere, L., Luong, N. T., Boily, J.-F., and Hanna, K.: Mineral Nanoparticle Aggregation Alters Contaminant Transport under Flow, *Environ. Sci. Technol.*, 57, 2415-2422, <https://doi.org/10.1021/acs.est.2c09358>, 2023.
- 875